Nanoscintillator coating: a key parameter that strongly impacts internalization, biocompatibility, and therapeutic efficacy in pancreatic cancer models

Clémentine Aubrun Fulbert, Fréderic Chaput, Sarah Stelse-Masson, Maxime Henry, Benoit Chovelon, Sylvain Bohic, Dennis Brueckner, Jan Garrevoet, Christine Moriscot, Benoit Gallet, et al.

Nanoscintillator coating: a key parameter that strongly impacts internalization, biocompatibility and therapeutic efficacy in pancreatic cancer models

*Clémentine AUBRUN FULBERT *, Frédéric CHAPUT, Sarah STELSE-MASSON, Maxime HENRY, Benoit CHOVELON, Sylvain BOHIC, Dennis BRUECKNER, Jan GARREVOET, Christine MORISCOT, Benoit GALLET, Julien VOLLAIRE, Olivier NICOUD, Frédéric LEROUGE, Sandrine DENIS-QUANQUIN, Xavier JAURAND, Thibault JACQUET, Anthony NOMEZINE, Véronique JOSSERAND, Jean-Luc COLL, Jean-Luc RAVANAT, Hélène ELLEAUME [&] and Anne-Laure BULIN [&,]**

[&] equal contribution

Clémentine AUBRUN FULBERT
Université Grenoble Alpes, INSERM, UA 07 Synchrotron Radiation for Biomedicine, Grenoble, France
Université Grenoble Alpes, INSERM U 1209, CNRS UMR 5309, Team Cancer Targets and Experimental Therapeutics, Institute for Advanced Biosciences, 38000 Grenoble, France
Email : clementine.aubrunfulbert@gmail.com

Frédéric CHAPUT
Université de Lyon, École Normale Supérieure de Lyon, Université Claude Bernard Lyon 1, CNRS UMR 5182, Laboratoire de Chimie, 46 Allée d'Italie, F69364 Lyon, France

Sarah STELSE-MASSON
Université Grenoble Alpes, INSERM, UA 07 Synchrotron Radiation for Biomedicine, Grenoble, France
Université Grenoble Alpes, INSERM U 1209, CNRS UMR 5309, Team Cancer Targets and Experimental Therapeutics, Institute for Advanced Biosciences, 38000 Grenoble, France

Maxime HENRY
Université Grenoble Alpes, INSERM U 1209, CNRS UMR 5309, Team Cancer Targets and Experimental Therapeutics, Institute for Advanced Biosciences, 38000 Grenoble, France

Benoit CHOVELON
Université Grenoble Alpes, Département de Pharmacochimie Moléculaire, CNRS, UMR 5063, F-38041 Grenoble, France
Service de Biochimie SB2TE, Institut de Biologie et Pathologie, CHU Grenoble Alpes, Grenoble, France

Sylvain BOHIC
Université Grenoble Alpes, INSERM, UA 07 Synchrotron Radiation for Biomedicine, Grenoble, France
ESRF – The European Synchrotron Radiation Facility, 38043 Grenoble, France

Dennis BRUECKNER, Jan GARREVOET
Deutsches Elektronen-Synchrotron DESY, Notkestr. 85, 22607 Hamburg, Germany

Christine MORISCOT
Université Grenoble Alpes, Integrated Structural Biology Grenoble (ISBG), UAR 3518, CNRS, CEA, EMBL, 71 avenue des Martyrs, F-38042, Grenoble, France

Benoit GALLET
Université Grenoble Alpes, CEA, CNRS, Institut de Biologie Structurale (IBS), 38000 Grenoble, France

Julien VOLLAIRE, Olivier NICOUD
Université Grenoble Alpes, INSERM U 1209, CNRS UMR 5309, Team Cancer Targets and Experimental Therapeutics, Institute for Advanced Biosciences, 38000 Grenoble, France

Frédéric LEROUGE, Sandrine DENIS-QUANQUIN
Université de Lyon, École Normale Supérieure de Lyon, Université Claude Bernard Lyon 1, CNRS UMR 5182, Laboratoire de Chimie, 46 Allée d'Italie, F69364 Lyon, France

Xavier JAURAND
Université Lyon 1, Centre Technologique des Microstructures, F-69622, Villeurbanne, France

Thibault JACQUET
Université Grenoble Alpes, INSERM, UA 07 Synchrotron Radiation for Biomedicine, Grenoble, France
Université Grenoble Alpes, INSERM U 1209, CNRS UMR 5309, Team Cancer Targets and Experimental Therapeutics, Institute for Advanced Biosciences, 38000 Grenoble, France

Anthony NOMEZINE
Université Grenoble Alpes, INSERM, UA 07 Synchrotron Radiation for Biomedicine, Grenoble, France

Véronique JOSSERAND, Jean-Luc COLL
Université Grenoble Alpes, INSERM U 1209, CNRS UMR 5309, Team Cancer Targets and Experimental Therapeutics, Institute for Advanced Biosciences, 38000 Grenoble, France

Jean-Luc RAVANAT
Université Grenoble Alpes, CEA, CNRS, SyMMES UMR 5819, Grenoble, France

Hélène ELLEAUME
Université Grenoble Alpes, INSERM, UA 07 Synchrotron Radiation for Biomedicine, Grenoble, France

Anne-Laure BULIN
Université Grenoble Alpes, INSERM U 1209, CNRS UMR 5309, Team Cancer Targets and Experimental Therapeutics, Institute for Advanced Biosciences, 38000 Grenoble, France
Email: Anne-laure.bulin@inserm.fr

Keywords: Nanoscintillator, radiotherapy, pancreatic cancer, nanoparticle functionalization, radiation dose-enhancement, biocompatibility

Abstract text.

Pancreatic cancer is associated with a poor prognosis despite multimodal treatments. To improve the efficacy of radiotherapy, the use of nanoscintillators is emerging. Made of high-Z elements, they absorb X-rays more efficiently than tissues and can locally enhance the radiation dose provided they have accumulated near tumor cells. This study focuses on the role of the

coating, a key parameter that controls both *in vitro* and *in vivo* properties of nanoparticles, including their internalization, biocompatibility and therapeutic efficacy. Polyethylene glycol and tripolyphosphate molecules are used to coat lanthanum fluoride nanoscintillators, and their properties are evaluated on pancreatic cancer models. The experiments demonstrate a higher internalization of the nanoparticles when coated with tripolyphosphate, in both 2D and 3D culture models, correlating with greater efficacy under X-rays, which may be associated with higher radiation dose-enhancement. The nanoparticles were also injected intravenously in healthy or tumor-bearing mice in order to study their toxicity, pharmacokinetics and biodistribution. Despite a strong liver and spleen accumulation, especially for the tripolyphosphate-coated nanoparticles, no toxicity was observed for either coating. Because they show promising radiation dose-enhancement *in vitro* in both culture models and a limited toxicity *in vivo*, polyethylene glycol-coated nanoparticles are good candidates for biomedical applications.

1. Introduction

Pancreatic ductal adenocarcinoma (PDAC) is the seventh leading cause of cancer death worldwide, with a 5-year survival rate below 10%. [1] The steady rise in its incidence is partly attributed to an ageing population and lifestyle factors such as smoking, alcohol consumption and obesity. [2] Currently, the only curative treatment for PDAC is ablative surgery combined with adjuvant chemotherapy. [3] However, many patients are diagnosed at an advanced stage with an unresectable tumor, and new treatments are urgently needed.

Radiotherapy (RT) has been studied as an adjuvant treatment for PDAC, but remains controversial and is currently only recommended for borderline cases of resectable PDAC. [4,5] While one American study reported a survival benefit when patients received chemoradiotherapy versus chemotherapy only, [6] two European studies showed no benefit. [7,8] To improve the efficacy of RT for PDAC, one strategy is to specifically increase the dose delivered to the tumor. To this end, stereotactic body radiotherapy (SBRT) has shown promising results for PDAC, enabling good tumor control and increasing life expectancy compared to chemotherapy alone or to chemotherapy combined with conventional RT. [5,9,10] However, as SBRT occasionally induces high toxicity, [11] other approaches are needed to improve the dose contrast between tumor and healthy tissue. One strategy is to accumulate high-Z elements in the tumor before irradiation to induce the so-called radiation dose enhancement (RDE) effect. RDE is a physical effect intrinsically due to the presence of high-Z elements during X-ray exposure. These elements absorb orthovoltage (< 250 keV) X-rays more

efficiently than tissue through photoelectric interactions. When photoelectric interactions occur, secondary electrons, including photo- and Auger electrons, are produced. This additional production of secondary electrons due to the high atomic number elements is the source of the physical dose increase. The mean free path of the electrons varies from a few nanometers (Auger electrons) to a few tens of micrometers (photoelectrons) as they interact with tissue and lose their energy by locally generating additional reactive oxygen species. To characterize the physical increase in radiation dose, the dose enhancement factor (DEF) is often used. It represents the ratio between the dose in tissues loaded with high-Z elements and the dose in tissues without high-Z elements. For example, with a DEF of 1.5, a 2 Gy dose delivered in the presence of nanoparticles would have a therapeutic effect similar to that of 3 Gy delivered without nanoparticles. RDE was first observed in the 70s with iodine contrast agents [12–14] and revived twenty years ago when high-Z element nanoparticles (NPs) were synthesized. Several studies ranging from Monte Carlo simulations [15] to *in vitro* and *in vivo* studies, [16,17] [18] [19] [20] [21] [22,23] have demonstrated that such NPs could sensitize pancreatic cancer cells to X-rays when NPs made of thorium, [15] titanium, [16,17] manganese, [18] yttrium, [19] cerium, [20] gadolinium [21] and gold [22,23] were incubated with tumor cells. Various effects were reported to explain this efficacy, including increased production of DNA damage [16,18,21,22] and reactive oxygen species (ROS) [16,17,19,20] enhanced apoptosis, [16–20,23] reduced cell proliferation [17,22] and reduced survival fraction. [16,17,20,21] *In vivo* studies also demonstrated increased animal survival [17,21] and decreased tumor volumes. [16–21] Despite these encouraging results, the limited efficacy of RT in PDAC is thought to stem mainly from acquired radioresistance, potentially due to hypoxia or alterations in the DNA damage response, DNA repair machinery and cell cycle checkpoint controls. [24] Therefore, increasing the radiation dose may ultimately be insufficient and inducing combination effects relying on distinct biological pathways may be necessary.

Nanoscintillators composed of high-Z elements recently emerged as promising radiotherapeutics. These NPs down-convert X-rays into UV/visible light [25] and gained interest for biomedical applications when they were proposed to induce photodynamic therapy in deep tissue under X-ray irradiation. [26] Since then, nanoscintillators were mainly investigated to induce X-ray photodynamic therapy, [27] but also UV-C induced specific DNA damage [28,29] and more recently RDE. [30] As these three therapeutic effects are based on different mechanisms of action, nanoscintillators could help combat radioresistance by activating various potentially synergistic effects.

When designing nanotherapeutics, achieving site-specific bioavailability is challenged by several biological barriers at the systemic, microenvironmental and cellular level. [31] The size, shape, charge and coating of the nanotherapeutics have been identified to strongly impact their ability to successfully cross these barriers [32].

More specifically, the coating has been shown to directly influence NPs stability and dispersibility in biological media, cytotoxicity, [33] cellular uptake, [34] as well as *in vivo* biocompatibility, blood pharmacokinetics and biodistribution. [35,36] Like most nanotherapeutics, nanoscintillators are expected to accumulate in the tumor through enhanced permeability and retention (EPR) effect, which has been extensively described in the literature. [37,38] Recently, questions have been raised about the relevance of this effect, as it is unclear whether nanomedicines can promote tumor accumulation via the EPR effect compared to free drugs [39]. However, EPR effect has been confirmed in mouse models as well as in humans, to promote tumor accumulation in comparison with normal tissues, [39] which is the interesting property for nanoscintillators accumulation.

This study aims to decipher to what extent the coating can influence the biological properties of nanoscintillators and their in vitro therapeutic efficacy. To this end, a comprehensive study was carried out with two organic coatings namely sodium tripolyphosphate (TPP) and polyethylene glycol (PEG) chains, which is the gold standard coating used to reduce opsonization and guarantee stealth effect to nanotherapeutics. [40] Both coatings were used to functionalize cerium-doped lanthanum fluoride (LaF_3:Ce) nanoscintillators. LaF_3:Ce has long been investigated as a model scintillating material [41]. Approximately 10 years ago, nanoformulations of LaF_3:Ce were developed [42] and started gaining interest for biomedical applications because of their interesting scintillating properties [43]. More recently, we demonstrated that small LaF_3:Ce nanoparticles, synthesized by a solvothermal route, induced a potent RDE in glioblastoma models. [30] In this paper, the effect of two different coatings on the therapeutic efficacy of these LaF_3:Ce nanoparticles was investigated. The impact of the coating was first assessed *in vitro* on cell internalization, toxicity and therapeutic efficacy under X-rays, then *in vivo* on biocompatibility, blood pharmacokinetics and biodistribution. *In vitro* experiments were carried out on human pancreatic cancer cell lines grown as adherent monolayers (2D) and spheroids (3D), while *in vivo* experiments were conducted on healthy and mice bearing orthotopic pancreatic tumors.

2. Results

2.1. Characterization of LaF_3:Ce NPs that exhibit a pure crystal phase

The X-ray diffraction pattern of LaF_3:Ce NPs isolated in powder form showed distinct diffraction peaks whose positions and intensities match the standard pattern of pure hexagonal LaF_3 crystal (Tysonite structure, space group $P\bar{3}c1$; ICDD card 01-082-0690) (**Figure 1**A). No additional peak was observed, ruling out the existence of a secondary phase. The broadening of the diffraction peaks confirms the nanocrystalline nature of the powder.

After functionalization, transmission electron microscopy (TEM) images were acquired (Figure 1B) and highlighted the crystallinity and nano-disc morphology of LaF_3:Ce NPs coated with PEG (Figure 1B1) or TPP (Figure 1B2) molecules. Statistical analysis of several hundreds of NPs provided a mean diameter of 10 nm and a standard deviation of 3.5 nm. Forty-two discs were imaged at their edges to calculate the mean thickness, estimated at 3.8 nm with a standard deviation of 0.5 nm. High-resolution TEM images showed a monocrystalline structure with no twin boundary (Figure 1B1, 1B2). Also, while PEG-coated NPs appeared well-individualized (Figure 1B1), TPP-coated NPs tended to aggregate (Figure 1B2), which can be explained by the absence of steric repulsion when using TPP molecules, compared to PEG chains. In addition, phosphorus atoms in TPP molecules can interact wholly or partially with cations present on the surface of LaF_3:Ce NPs, thus providing a surface charge to the NPs. Finally, the electron diffraction pattern showed no other phases or impurities (Figure 1B3), consistently with the X-ray diffraction results.

The NPs composition evaluated by energy dispersive spectrometry (EDS) was in accordance with the targeted composition ($La_{0.9}Ce_{0.1}F_3$). It was confirmed by inductively coupled plasma mass spectrometry (ICP-MS) analysis that provided a lanthanum/cerium ratio of 8.73 (± 0.01, SEM) for PEG-coated NPs and 8.91 (± 0.04, SEM) for TPP-coated NPs.

Signals between 1350 and 1750 cm^{-1} and between 2650 and 3700 cm^{-1} on the spectra measured by total reflection Fourier transform infrared (ATR-FTIR) spectroscopy (Figure 1C, D), demonstrated that small organic capping molecules coming from the solvent (2-pyrrolidinone or its open form γ-aminobutyric acid) were present on the surface of the NPs. ATR-FTIR spectroscopy was then used to demonstrate the effective grafting of PEG (Figure 1C) or TPP (Figure 1D) groups on the surface of the NPs. After PEGylation, the infrared spectrum (Figure 1C, blue) showed typical signatures of PEG species, with bands at 2880 cm^{-1} and around 1100 cm^{-1} for ether, C–H and C–O–C stretching modes, respectively. The bands assigned to solvent molecules were no longer present. After TPP grafting, the infrared spectrum (Figure 1D, blue) showed the infrared absorption bands of the triphosphoric acid salt, replacing the bands of the solvent molecules. The FTIR spectrum of pure sodium TPP showed

characteristic bands at 1218 cm^{-1} (stretching vibration of P=O), 1136 cm^{-1} (symmetric and anti-symmetric stretching vibration of O−P=O), 1091 cm^{-1} (symmetric and asymmetric stretching vibration of the PO_3) and 886 cm^{-1} (stretching vibration of P−O−P bridge). [44] The amount of ligand on the NP surface was assessed by thermogravimetric analysis. The sample of PEGylated NPs showed a significant mass loss (≈ 30%) in the 150°C-400°C range, attributed to the decomposition of the organic part. On the contrary and as expected, a small mass loss (< 4%) was observed for the NPs with the inorganic TPP ligand. The coated NPs were also analyzed by Nuclear Magnetic Resonance (NMR), in solution in deuterated water. The ^{31}P spectrum in solution confirmed the presence of PEG and TPP at the surface of the NPs (**Figure S1**, **Figure S2**).

The stability of the NPs was evaluated by dynamic light scattering (DLS) performed on LaF_3:Ce NPs suspended in phosphate buffer saline (PBS), culture medium and mouse plasma. In PBS, the hydrodynamic diameter of LaF_3:Ce NPs was 22 nm with a polydispersity index (PDI) of 0.19 for PEG-coated NPs (Figure 1E), and 180 nm with a PDI of 0.32 for the TPP-coated NPs (Figure 1F). These results were consistent with the TEM images that showed well-dispersed PEG-coated NPs and aggregated TPP-coated NPs. Unlike PEG-coated NPs that were stable regardless of the medium (hydrodynamic diameter < 45 nm, PDI < 0.45), TPP-coated NPs tended to aggregate in culture medium (hydrodynamic diameter = 790 nm, PDI = 0.55) and mouse plasma (hydrodynamic diameter = 257 nm, PDI = 0.90).

Zeta potentials (ζ) measured in PBS were - 2.24 mV and - 23.13 mV for PEG- and TPP-coated NPs, respectively.

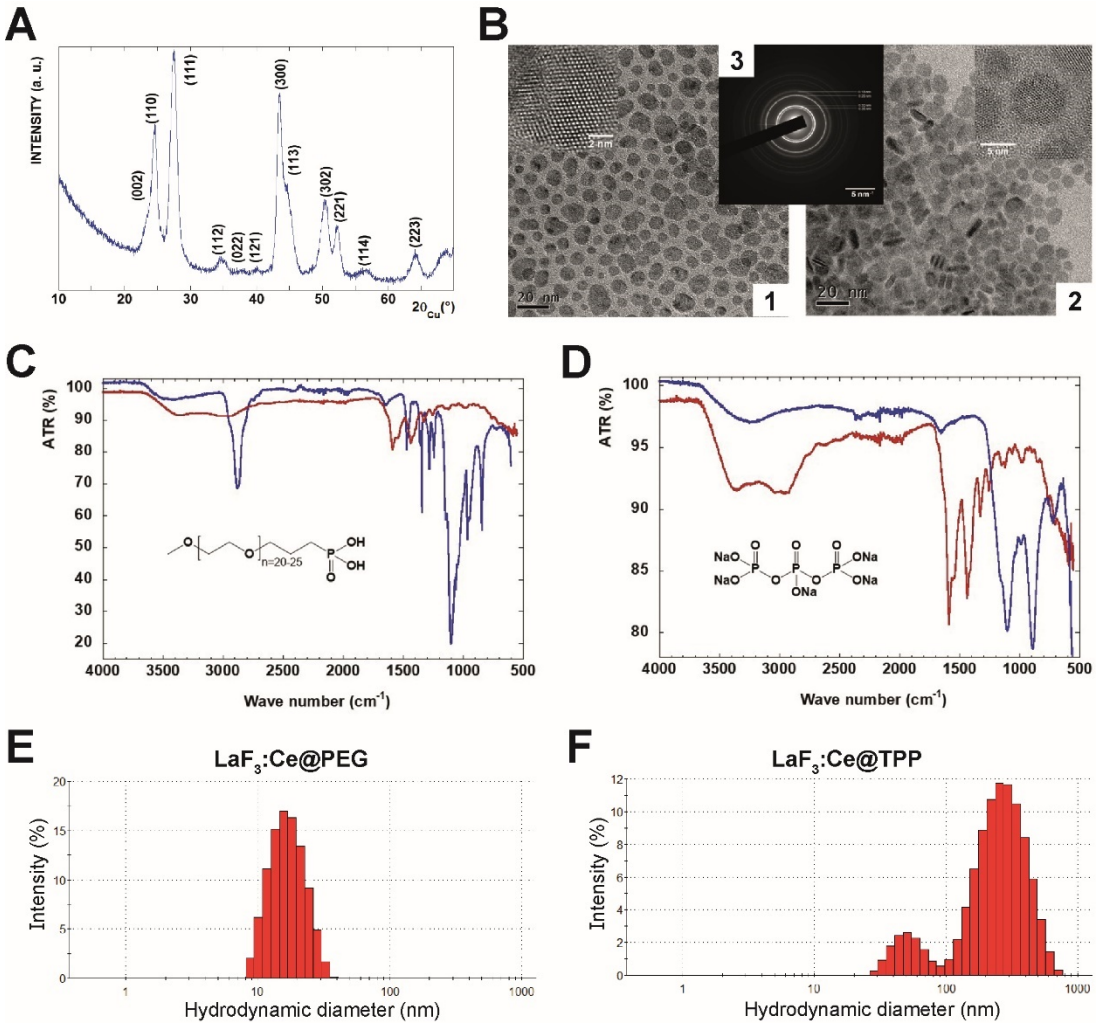

Figure 1. PEG- and TPP-coated LaF_3:Ce NPs were successfully synthesized. A) X-ray diffraction pattern of LaF_3:Ce nanopowder solvothermally obtained in 2-Pyrrolidinone at 170°C for 1 hour. **B)** TEM images of LaF_3:Ce NPs after surface modification with PEG (1) or TPP (2) molecules, scale = 20 nm. Electronic diffraction of nanodiscs (3), scale = 5 nm. **C)** FTIR-ATR spectra of the LaF_3:Ce NPs before (red) and after (blue) PEGylation. **D)** FTIR-ATR spectra of the LaF_3:Ce NPs before (red) and after (blue) TPP grafting. **E, F)** Hydrodynamic diameters of LaF_3:Ce NPs in PBS with PEG (E) and TPP (F) coating, measured by DLS.

2.2. LaF_3:Ce NPs accumulate in cytoplasmic vesicles and TPP-coated NPs are more efficiently internalized compared to PEG-coated NPs

LaF_3:Ce NPs are only fluorescent upon far-UV or X-ray excitation and cannot be imaged by classical confocal microscopy. To visualize their intracellular distribution, two complementary methods were used: X-ray fluorescence (XRF) microscopy and TEM. Whereas XRF microscopy is quantitative (**Figure S3**), it does not provide confocal resolution and therefore,

does not inform about the actual internalization of the NPs. On the contrary, TEM only provides a qualitative localization of the NPs visualized as dark spots.

XRF images depict zinc (nucleus, green), potassium (cytoplasm, blue), and lanthanum (LaF_3:Ce NPs, red) (**Figure 2**A1, 2A4) and show an accumulation of NPs as small and large clusters for PEG- and TPP-coated NPs, respectively (Figure 2A2, 2A5). XRF data showed a stronger accumulation of lanthanum for TPP- than PEG-coated NPs and a specific accumulation of the NPs in lysosomes, especially when coated with TPP (Figure 2A3, 2A6, **Figure S4**). TEM images confirmed the accumulation of the NPs in cytoplasmic vesicles (Figure 2B, 2C) and a stronger internalization of TPP- compared to PEG-coated NPs.

2.3. LaF_3:Ce NPs diffuse throughout the spheroid and accumulate well withing 3D models

XRF microtomography performed on PANC-1 spheroids provided qualitative and quantitative distribution of zinc and lanthanum. The computed tomography (CT) images showed that NPs were able to diffuse through the spheroids. Moreover, TPP-coated NPs accumulated 11.5-fold more than PEG-coated NPs in the spheroids, with lanthanum concentrations of 1.6 $mg.cm^{-3}$ and 0.14 $mg.cm^{-3}$, respectively.

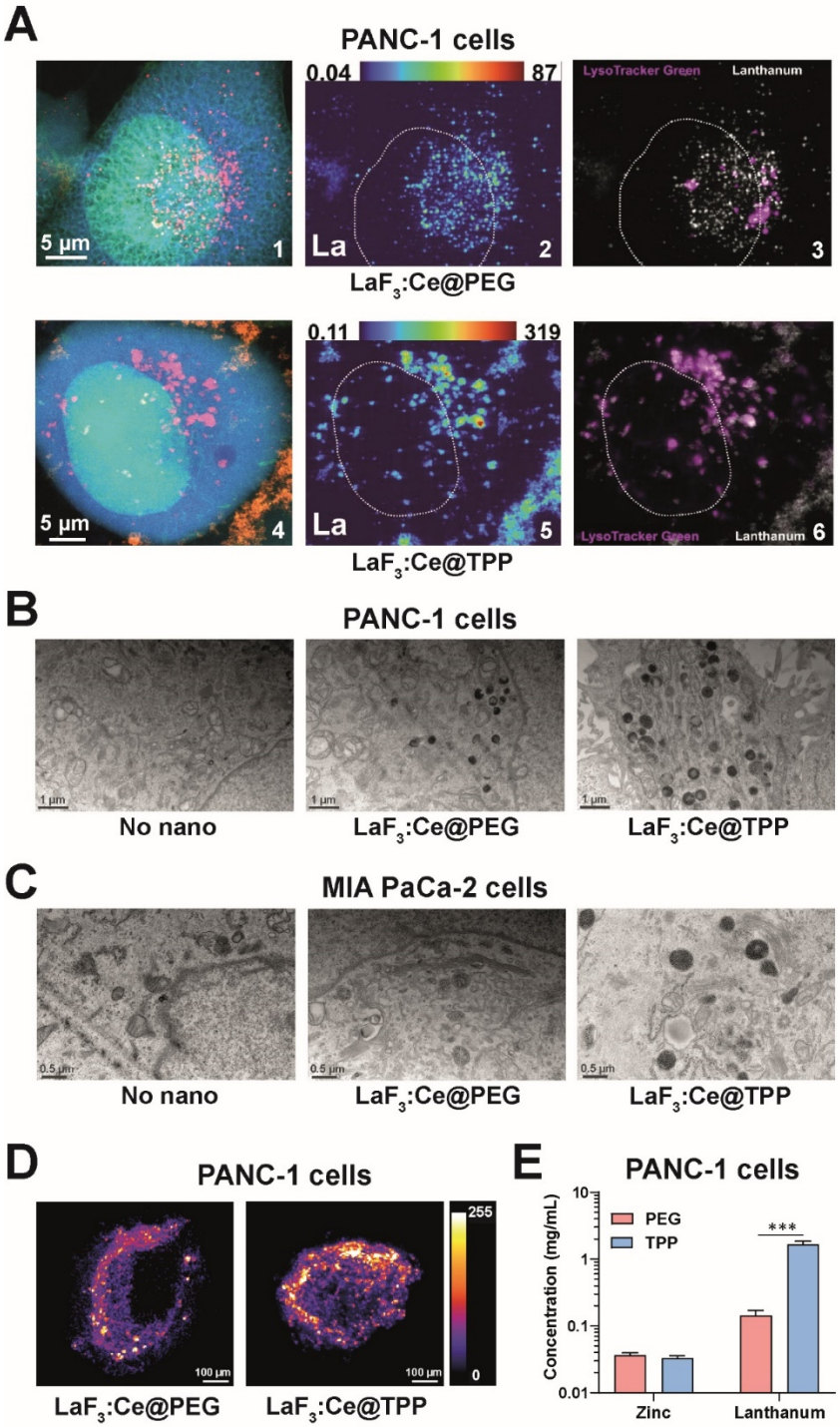

Figure 2. LaF_3:Ce NPs internalize in lysosomes and diffuse throughout spheroids. A) XRF images of PANC-1 cells previously incubated for 24 hours with 0.1 $mg.mL^{-1}$ PEG- (1, 2, 3) or TPP- (4, 5, 6) coated NPs (scale = 5 µm). 1, 4) zinc (nucleus, green), potassium (cytoplasm, blue) and lanthanum (NPs, red). 2, 5) lanthanum. 3, 6) lysosomes (lysotracker green, purple) and lanthanum (NPs, white). **B, C)** TEM images of PANC-1 (B, scale = 1 µm) and MIA PaCa-2 cells (C, scale = 0.5 µm) incubated for 24 hours with PBS or 0.1 $mg.mL^{-1}$ NPs. **D)** CT images of X-ray fluorescence emission of lanthanum (XRF) in PANC-1 spheroids incubated for

24 hours with 0.1 mg.mL^{-1} NPs (scale = 100 µm). **E)** Zinc (cell) and lanthanum concentrations quantified using the XRF microtomography images.

2.4. LaF_3:Ce NPs show no toxicity on cells grown as monolayers when incubated for 24 hours at concentrations up to 1 mg.mL^{-1} in culture medium

MTS assays were performed on PANC-1 (**Figure 3**A) and MIA PaCa-2 (Figure 3B) cells incubated 24 hours with increasing concentrations of NPs. Cell viability stayed above 95% for concentrations of up to 1 mg.mL^{-1}. IC_{50} values measured on PANC-1 cells reached 4.7 mg.mL^{-1} and 2.9 mg.mL^{-1} for PEG- and TPP-coated NPs, respectively, whereas on MIA PaCa-2 cells, they reached 5.6 mg.mL^{-1} and 4.0 mg.mL^{-1} for PEG- and TPP-coated NPs, respectively.

2.5. TPP-coated LaF_3:Ce NPs induce a stronger RDE effect in monolayers than PEG-coated NPs

Because RDE effect strongly depends on the intracellular concentration in heavy elements, [45] two incubation conditions were compared: 24 hours at 1 mg.mL^{-1} (Figure 3C) and 1 hour at 5 mg.mL^{-1} (Figure 3D). The lanthanum and cerium concentrations were measured by ICP-MS. After 1 hour incubation with 5 mg.mL^{-1}, intracellular accumulation of lanthanum was 9- and 62-times higher for TPP- versus PEG-coated NPs for PANC-1 and MIA PaCa-2 cells, respectively (**Table S1**, Figure 3D). After 24-hours incubation with 1 mg.mL^{-1}, these ratios decreased to 3.5 and 1.4 for PANC-1 and MIA PaCa-2 cells, respectively (Figure 3C). Similar results were obtained for cerium (**Figure S5**) and the ratios between lanthanum and cerium concentrations were close to the expected value of 9. The therapeutic efficacy of LaF_3:Ce NPs was assessed by clonogenic assays after 1-hour incubation at 5 mg.mL^{-1} (Figure 3E). Whatever the coating, the NPs strongly enhanced the effect of X-ray irradiation on PANC-1 cells, whose ability to proliferate was severely impaired (Figure 3F, G). However, only the TPP-coated NPs significantly decreased the proliferation of MIA PaCa-2 cells after X-ray irradiation (Figure 3H, I). Experimental dose-enhancement factors (DEFs) were calculated using linear quadratic regression fits applied to the survival data, as detailed in **SI.6**. The radiobiologic α and β parameters extracted from these fits are presented **Table 1.**

	Control			LaF_3:Ce@PEG				LaF_3:Ce@TPP			
	α (Gy^{-1})	β (Gy^{-2})	α/β (Gy)	α (Gy^{-1})	β (Gy^{-2})	α/β (Gy)	DEF	α (Gy^{-1})	β (Gy^{-2})	α/β (Gy)	DEF
PANC-1	0.12	0.07	1.62	0.10	0.13	0.80	1.24	0.14	0.16	0.85	1.45
MIA PaCa-2	0.07	0.14	0.53	0.00	0.17	0.00	1.03	0.36	0.20	1.75	1.42

Table 1. Linear quadratic parameters and DEFs extracted from clonogenic assays.

For PANC-1, the α/β ratio decreased in presence of PEG- or TPP-coated NPs compared to the controls. For MIA PaCa-2, this ratio decreased to almost 0 with PEG-coated NPs and strongly increased with TPP-coated NPs. With PEG-coated NPs, the RDE effect occurred only for PANC-1, with a calculated DEF of 1.24 versus 1.03 for MIA PaCa-2. In contrast, TPP-coated NPs induced a strong RDE effect for both cell lines, with DEFs of 1.45 and 1.42 for PANC-1 and MIA PaCa-2, respectively.

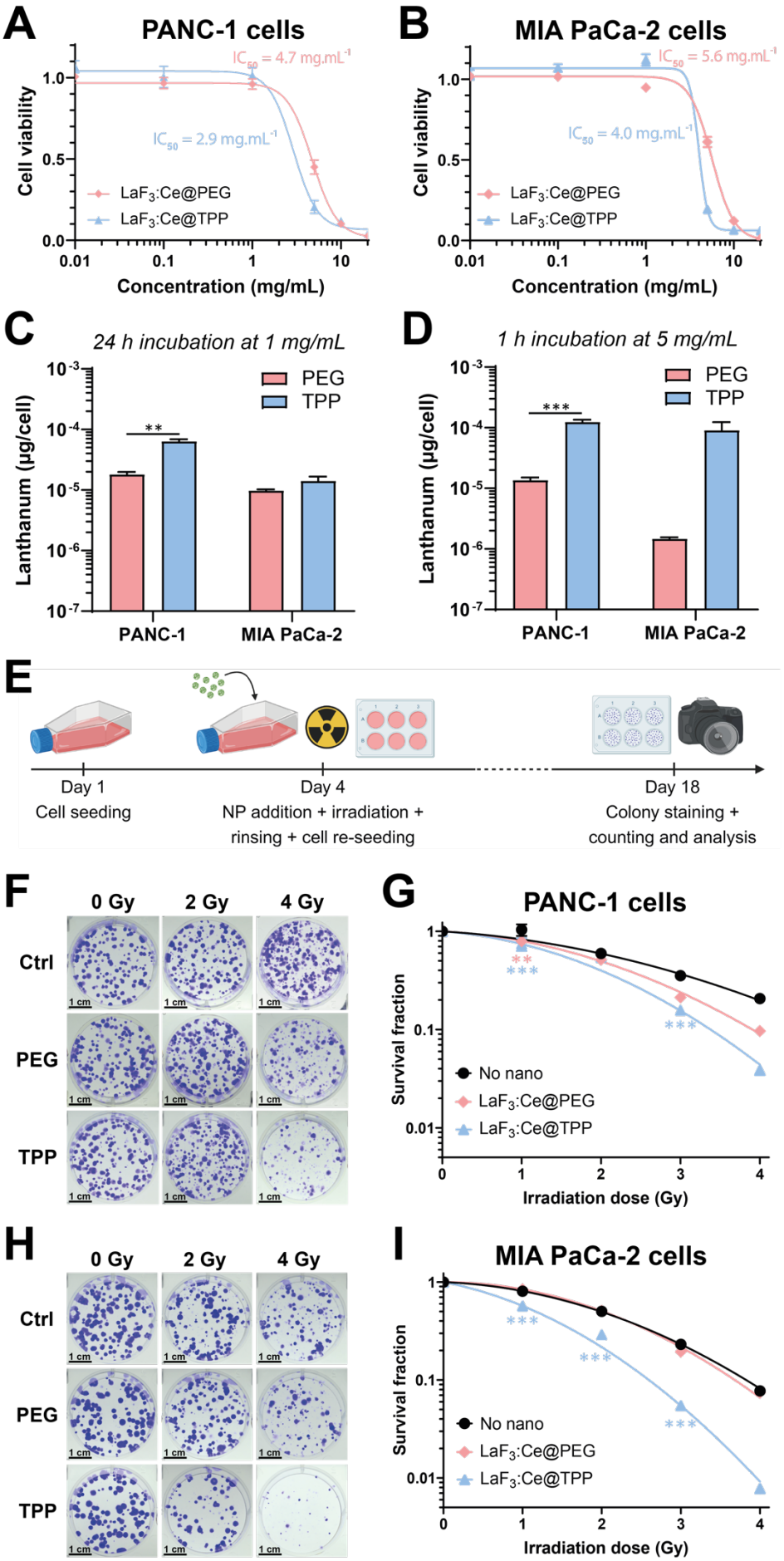
A
PANC-1 cells
IC50 = 4.7 mg.mL-1
IC50 = 2.9 mg.mL-1
LaF3:Ce@PEG
LaF3:Ce@TPP
Cell viability
Concentration (mg/mL)
B
MIA PaCa-2 cells
IC50 = 5.6 mg.mL-1
IC50 = 4.0 mg.mL-1
LaF3:Ce@PEG
LaF3:Ce@TPP
Cell viability
Concentration (mg/mL)
C
24 h incubation at 1 mg/mL
PEG
TPP
Lanthanum (µg/cell)
PANC-1
MIA PaCa-2
D
1 h incubation at 5 mg/mL
PEG
TPP
Lanthanum (µg/cell)
PANC-1
MIA PaCa-2
E
Day 1
Cell seeding
Day 4
NP addition + irradiation +
rinsing + cell re-seeding
Day 18
Colony staining +
counting and analysis
F
0 Gy
2 Gy
4 Gy
Ctrl
PEG
TPP
G
PANC-1 cells
Survival fraction
No nano
LaF3:Ce@PEG
LaF3:Ce@TPP
Irradiation dose (Gy)
H
0 Gy
2 Gy
4 Gy
Ctrl
PEG
TPP
I
MIA PaCa-2 cells
Survival fraction
No nano
LaF3:Ce@PEG
LaF3:Ce@TPP
Irradiation dose (Gy)

Figure 3. LaF_3:Ce NPs induce a strong RDE effect in 2D cultures. A, B) Cell viability after incubation with increasing doses of NPs in PANC-1 (A) and MIA PaCa-2 cells (B) assessed by MTS. Non-linear regression fits: [inhibitor] vs response model. **C, D)** Lanthanum concentration measured in each cell line by ICP-MS after 24 hours incubation with 1 $mg.mL^{-1}$ NPs (C) or 1 hour incubation with 5 $mg.mL^{-1}$ NPs (D). **E)** Timeline of the clonogenic assay: cells were incubated with 5 $mg.mL^{-1}$ NPs for 1 hour, irradiated with X-ray, rinsed and seeded for colony formation. Created with BioRender.com. **F-I)** Representative images of PANC-1 (F) and MIA PaCa-2 (H) colonies stained with crystal violet (scale = 1 cm). Survival fraction calculated for PANC-1 (G) and MIA PaCa-2 (I) cells. Data were normalized on the 0 Gy condition and fitted with the linear quadratic cell death model. (*) indicates $p < 0.05$, (**) indicates $p < 0.01$, and (***) indicates $p < 0.001$.

2.6. Tumor spheroids can be safely incubated for 24 hours with 1 $mg.mL^{-1}$ NPs.

A live/dead assay was used to evaluate the viability of tumor spheroids previously incubated for 24 hours with increasing concentrations of LaF_3:Ce NPs (**Figure 4**A, B). [30,46] PEG-coated NPs are well tolerated (viability >95%) up to 2.5 $mg.mL^{-1}$. TPP-coated NPs started to affect the spheroid viability for concentrations above 1 $mg.mL^{-1}$. For NP concentrations ≥ 10 $mg.mL^{-1}$, the spheroids lost their integrity, making viability analysis impossible (data not shown). IC_{50} values were calculated for PEG- and TPP-coated NPs and reached, respectively, 6.4 $mg.mL^{-1}$ and 2.7 $mg.mL^{-1}$ for PANC-1 spheroids, and 5.4 $mg.mL^{-1}$ and 3.0 $mg.mL^{-1}$ for MIA PaCa-2 spheroids.

2.7. TPP-coated NPs accumulate more efficiently in tumor spheroids than PEG-coated NPs

After 24 hours incubation with 1 $mg.mL^{-1}$ NPs, the concentration of lanthanum accumulated in spheroids was assessed by ICP-MS (Figure 4C, D; **Table S1**). TPP-coated NPs accumulated significantly more compared to PEG-coated NPs: 71-times more in PANC-1 spheroids (Figure 4C) and a 122-times more in MIA PaCa-2 spheroids (Figure 4D). However, the concentrations measured for TPP-coated NPs are probably overestimated due to experimental difficulties of collecting the spheroids without simultaneously harvesting NPs aggregates, which remained in suspension despite the washing steps. For each condition, the lanthanum/cerium ratio was between 8.6 and 8.9, in agreement with the expected value of 9.

2.8. LaF_3:Ce NPs induce a significant RDE effect in tumor spheroids

To assess the RDE effect induced by LaF_3:Ce NPs in spheroids, live/dead assays were performed (Figure 4E). After 24-hours incubation with 1 $mg.mL^{-1}$ NPs, spheroids were exposed to increasing doses of X-rays (0 to 12 Gy). LaF_3:Ce NPs significantly reduced spheroid viability with both coatings in PANC-1 spheroids (Figure 4F, G) and with TPP-coating only in MIA PaCa-2 spheroids (Figure 4H, I). A significant, yet milder effect, was reported for PEG-coated NPs in MIA PaCa-2 spheroids (Figure 4H, I). PEG- and TPP-coated NPs also increased spheroid necrosis upon X-ray irradiation for both cell lines (**Figure S6**), whereas spheroid size was only reduced by PEG-coated NPs for PANC-1 spheroids (**Figure S7**). DEFs were calculated using the slope (γ parameter) extracted from the linear regression models applied to the spheroid viability data; DEF and γ parameters are provided in **Table** .

	Control	LaF_3:Ce@PEG		LaF_3:Ce@TPP	
	γ (Gy^{-1})	γ (Gy^{-1})	DEF	γ (Gy^{-1})	DEF
PANC-1	0.021	0.036	1.73	0.044	2.08
MIA PaCa-2	0.018	0.023	1.25	0.031	1.70

Table 2: Simple linear parameters and DEFs

Both PEG- and TPP-coated NPs induced a strong RDE, with DEFs of 1.73 and 2.08 for PANC-1 spheroids, and 1.25 and 1.70 for MIA PaCa-2 spheroids, respectively. For both cell lines, the experimental DEFs were higher with TPP-coated NPs compared to PEG-coated ones.

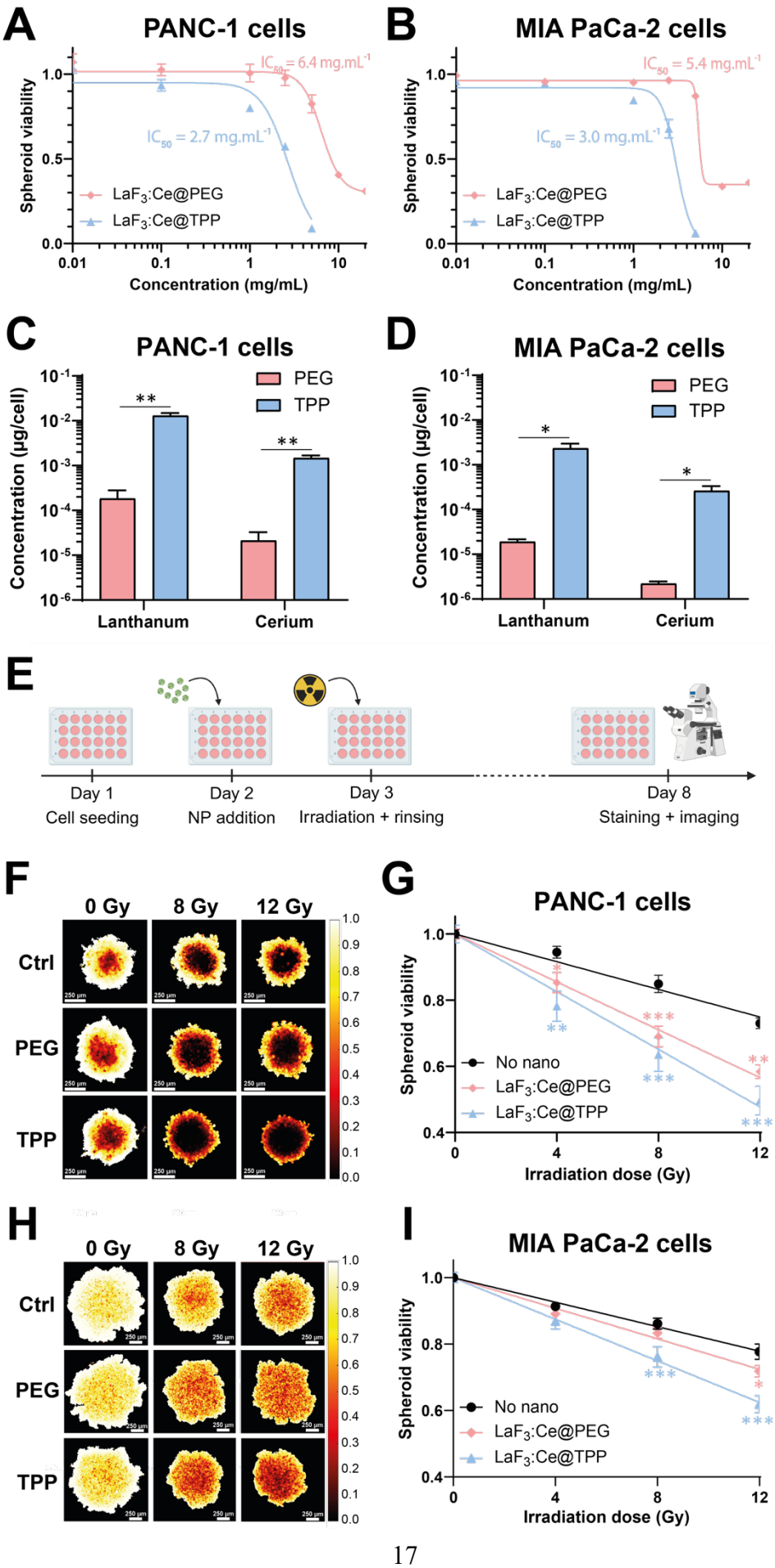
A
PANC-1 cells
Spheroid viability
IC50 = 6.4 mg.mL-1
IC50 = 2.7 mg.mL-1
LaF3:Ce@PEG
LaF3:Ce@TPP
Concentration (mg/mL)
B
MIA PaCa-2 cells
IC50 = 5.4 mg.mL-1
IC50 = 3.0 mg.mL-1
C
PANC-1 cells
Concentration (µg/cell)
PEG
TPP
Lanthanum
Cerium
D
MIA PaCa-2 cells
E
Day 1
Cell seeding
Day 2
NP addition
Day 3
Irradiation + rinsing
Day 8
Staining + imaging
F
0 Gy
8 Gy
12 Gy
Ctrl
PEG
TPP
G
PANC-1 cells
No nano
Irradiation dose (Gy)
H
I
MIA PaCa-2 cells

Figure 4. LaF_3:Ce NPs induce a strong RDE effect in pancreatic tumor spheroids. A, B) Viability of PANC-1 (A) and MIA PaCa-2 (B) spheroids previously incubated with increasing concentrations of LaF_3:Ce NPs, measured using a live/dead assay. Data were adjusted using a non-linear [inhibitor] vs response model. **C, D)** Lanthanum and cerium concentrations measured by ICP-MS in PANC-1 (C) and MIA PaCa-2 (D) spheroids. **E)** Timeline used to assess the therapeutic effect of NPs under X-ray in tumor spheroids: after 24 hour incubation with 1 $mg.mL^{-1}$ NPs, spheroids were irradiated, rinsed and maintained for 5 days before undergoing a live/dead assay. Created with BioRender.com. **F, H)** Representative viability heatmaps of PANC-1 (F) and MIA PaCa-2 (H) spheroids irradiated at 0, 8 and 12 Gy (scale = 250 µm). **G, I)** Spheroid viability of PANC-1 (G) and MIA PaCa-2 (I) spheroids. Data were normalized on the 0 Gy condition; linear regression fits were applied. (*) indicates $p < 0.05$, (**) indicates $p < 0.01$, and (***) indicates $p < 0.001$.

2.9. DEF correlates with lanthanum concentration in 2D and 3D models.

The experimental DEF measured from the clonogenic or the spheroids assays were plotted as a function of the intracellular lanthanum concentration measured by ICP-MS (**Figure 5**). A semi log function fitted the data with a R-Squared (R^2) coefficient of 0.92 and 0.99 for the PANC-1 and MIA PaCa-2 cells, respectively, demonstrating a strong correlation between the intra-cellular, or intra-spheroid lanthanum concentration and the dose-enhancement factor.

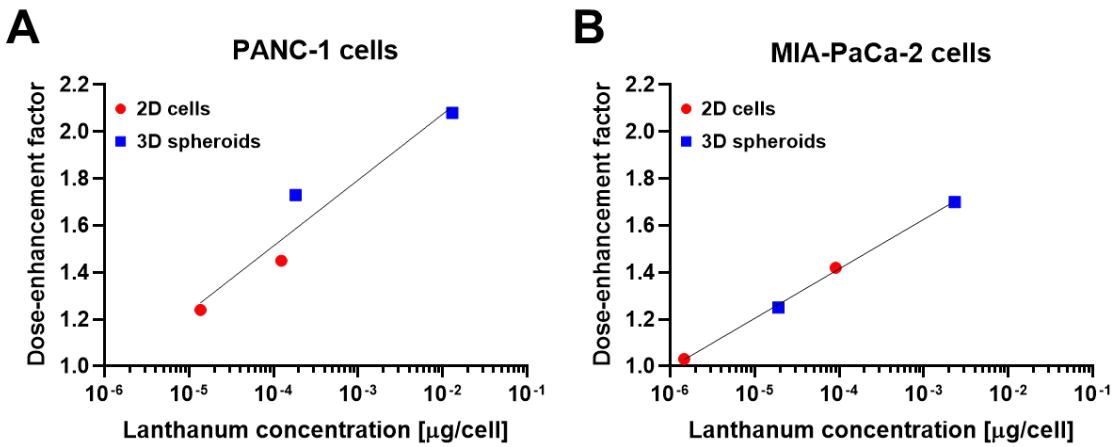

Figure 5. Experimental DEF plotted as a function of the lanthanum concentration measured by ICP-MS in 2D (red dots) and 3D (blue squares) models. Results are shown for PANC-1 (A) and MIA PaCa-2 (B) cells.

2.10. LaF_3:Ce NPs are safe to inject intravenously in healthy mice up to 200 $mg.kg^{-1}$

Intravenous (iv) injection of 200 $mg.kg^{-1}$ PEG- or TPP-coated NPs induced no alteration in mice body weight (**Figure S8**), signs of pain, nor changes in behavior or survival.

2.10.1. LaF_3:Ce NPs tend to accumulate in the liver and spleen of healthy mice

NPs mainly accumulated in the liver and spleen, as measured by ICP-MS (**Figure 6**A). 24 hours after injection, 62%ID.g^{-1} (percent injected dose per gram of tissue) and 37%ID.g^{-1} lanthanum were measured in the liver for PEG- and TPP-coated NPs, respectively. These values reached 42%ID.g^{-1} 14-days post-injection for both coatings. In the spleen, the coating strongly influenced the uptake as 45%ID.g^{-1} and 152%ID.g^{-1} lanthanum were measured 24 hours post-injection for PEG- and TPP-coated NPs, respectively. These values only slightly decreased over 14 days. Lanthanum was also found in the kidney with a higher concentration for PEG-coated NPs and in the lungs with a higher concentration for TPP-coated. Over time, lanthanum concentration decreased in the kidney, yet remained stable in the lungs.

2.10.2. Injection of 200 mg.kg^{-1} LaF_3:Ce NPs did not severely impared plasma biochemistry

Biochemistry analysis was performed on plasma collected 24 hours and 14 days after the injection of 200 mg.kg^{-1} LaF_3:Ce NPs (Figure 6B-F). After 24 hours, no significant effect was reported on any of the measured parameters. After 14 days, ALAT and ASAT levels were significantly increased by PEG- or TPP-coated NPs and by TPP-coated NPs, respectively (Figure 6C). No significant change was observed in any other functions.

2.11. PEG-coated NPs circulate twice as long as TPP-coated NPs in the blood

The pharmacokinetic profile of LaF_3:Ce NPs was evaluated by ICP-MS. It showed progressive elimination from the bloodstream over time, for both PEG- (Figure 6G) and TPP-coated NPs (Figure 6H). The elimination half-life in blood was 2 hours and 1 hour for PEG- and TPP-coated NPs, respectively. Not only did PEG-coated NPs circulate longer than TPP-coated NPs, but the concentration of lanthanum in blood 5 minutes after injection was also much higher, with 25%ID.g^{-1} versus less than 1%ID.g^{-1}.

2.12. PEG-coated NPs accumulate more efficiently in orthotopic tumors than TPP-coated NPs

The biodistribution of LaF_3:Ce NPs intravenously injected was investigated in an orthotopic model of pancreatic cancer (Luc-PANC-1 cells) implanted in nude mice. Tumor implantation did not alter mice body weight (**Figure S9**) nor induced signs of pain, changes in behavior or in survival. NPs were injected 35 days post-implantation, after the randomization of animals based on tumor size (Figure 6I). As for healthy mice, both PEG- (Figure 6J) and TPP-coated

NPs (Figure 6K) mainly accumulated in the liver and spleen. One-hour post-injection, TPP-coated NPs were found in higher amounts compared to PEG-coated ones, with lanthanum concentrations of 62 and 6%ID.g^{-1} in the spleen, and 29 and 13%ID.g^{-1} in the liver, respectively. For PEG-coated NPs, the lanthanum concentration increased over time in liver and spleen, whereas it decreased in heart, lungs and kidney. The highest tumor accumulation was measured 4 hours after injection and reached 1.4%ID.g^{-1}. For TPP-coated NPs, there was no significant change in the lanthanum accumulation over time. The highest tumor accumulation was also obtained 4 hours post-injection and reached 0.6%ID.g^{-1}.

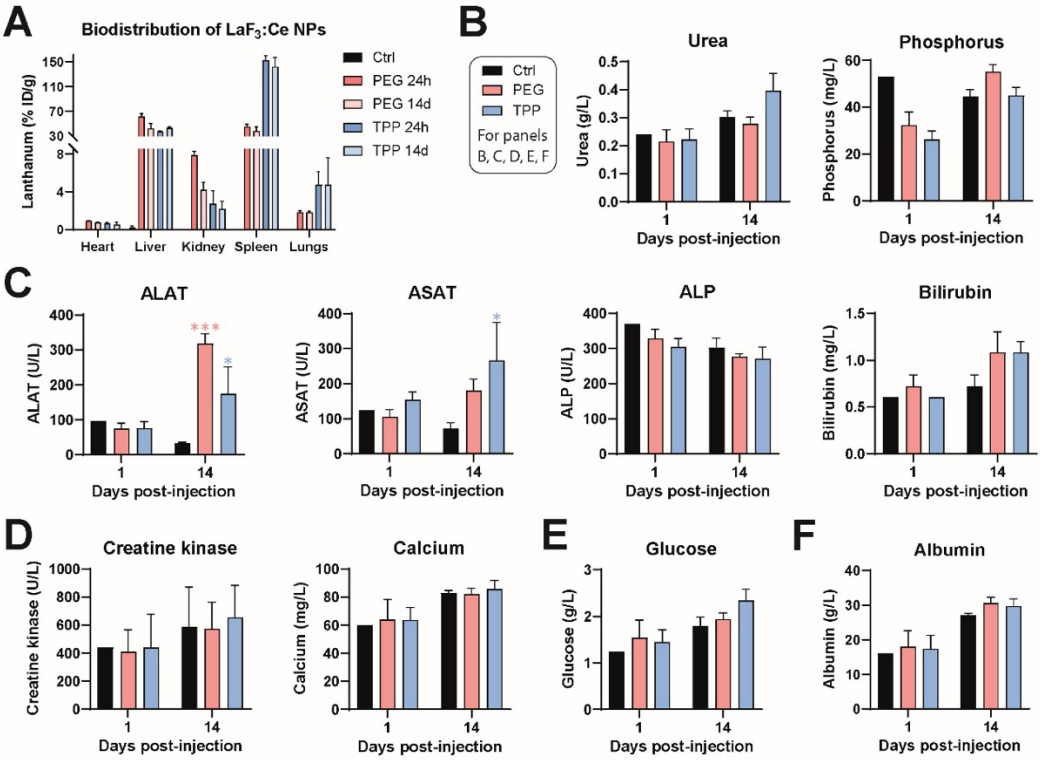

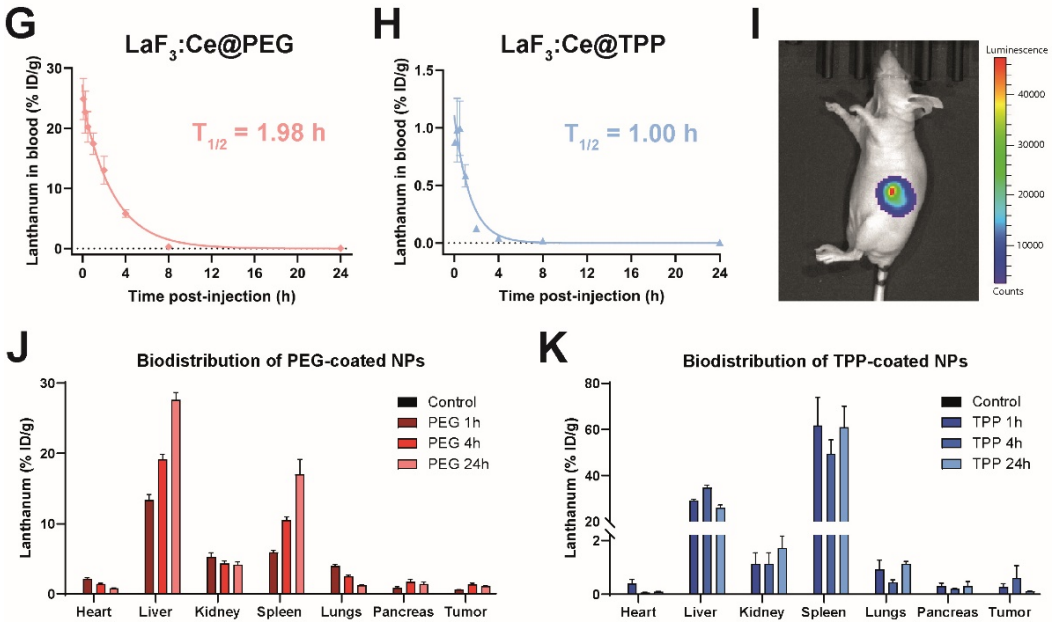

Figure 6. LaF_3:Ce NPs can safely be intravenously injected in mice at 200 mg.kg^{-1}. A) Biodistribution of PEG- and TPP-coated NPs after intravenous injection in BALB/c mice, N = 3 mice/group. Lanthanum concentration was measured by ICP-MS in organs collected 24 hours and 14-day after injection, and normalized as %ID.g^{-1} in tissue. **B-F)** Plasma biochemistry on blood samples collected 24 hours and 14-days post-injection. Analyses were related to renal (B), hepatic (C) and muscular functions (D), metabolism (E) and nutritional status (F), N = 5 mice/group. ALAT, alanine transaminase; ASAT, aspartate transaminase; ALP, alkaline phosphatase. **G, H)** Pharmacokinetic profile of PEG- (G) and TPP-coated (H) NPs, N = 3 mice/group. Lanthanum concentration in blood was measured by ICP-MS and normalized as %ID.g^{-1} in blood. A two-phase decay model was used to fit the data. **I)** Representative bioluminescence image of a tumor-bearing mouse acquired 34 days after orthotopic implantation of Luc-PANC-1 cells. **J, K)** Biodistribution of PEG- (J) and TPP-coated NPs (K) after injection in tumor-bearing mice, N = 5 mice/group. Tissues were collected 1-, 4- and 24-hours after injection and analyzed by ICP-MS.

3. Discussion

2D cell culture models were used to investigate uptake mechanisms of LaF_3:Ce NPs. Both XRF microscopy and TEM imaging showed their accumulation in lysosomes. However, the coating had a strong influence on their behavior: as TPP-coated NPs aggregate more than PEG-coated NPs, and are better internalized by tumor cells. Altogether, these results point to an absorption mechanism by endocytosis. ICP-MS quantitatively confirmed qualitative TEM observations: TPP-coated NPs are absorbed more efficiently than PEG-coated NPs in both cell lines.

Internalization kinetics were also affected by the coating, with TPP-coated NPs accumulating more rapidly in cells. These findings could be explained by the larger hydrodynamic diameter and higher absolute charge of TPP-coated NPs compared to PEG-coated NPs. These differences in efficacy and speed of internalization may explain several observations. First, it can justify why a similar concentration of NPs in culture medium leads to a higher toxicity with TPP-coated NPs compared to PEG-coated NPs. This also correlates well with the higher DEF observed in clonogenic assays when accumulation of NPs is greatest, after 24 hours incubation with 5 $mg.mL^{-1}$ NPs, in agreement with the literature. [45,47] The only incubation condition for which no RDE was observed is associated with the lowest lanthanum uptake (MIA PaCa-2 cells incubated with PEG-coated NPs). 3D models used to evaluate the ability of NPs to penetrate tumor spheroids provided similar trends to those observed in 2D models. XRF measurements demonstrated that TPP-coated NPs accumulated in higher concentration in spheroids than PEG-coated NPs. For both coatings, a fluorescence signal from the core of the spheroids was detected, demonstrating the diffusion of NPs in spheroids. Measurements of lanthanum and cerium concentrations using XRF microtomography and ICP-MS showed that TPP-coated NPs internalized more efficiently in spheroids than PEG-coated NPs. However, as previously mentioned, concentrations measured by ICP-MS for TPP-coated NPs may have been over-estimated. Treatment efficacy was evaluated at the highest non-toxic concentration determined beforehand: 24 hours with 1 $mg.mL^{-1}$ NPs. Live/dead assays demonstrated a significant radiation dose-enhancement for both cell lines, with a decrease in spheroid viability, more pronounced with TPP- compared to PEG-coated NPs. In addition, while spheroid necrosis was induced by both types of NPs upon X-ray irradiation in PANC-1 spheroids, PEG-coated NPs were more efficient in MIA PaCa-2 ones. Regarding the effect on spheroid size, X-ray irradiated PEG-coated NPs only reduced the size of PANC-1 spheroids. The enhanced therapeutic efficacy observed in PANC-1 spheroids can be related to the greater accumulation of NPs. Indeed, a strong correlation was observed between the experimental DEF and the lanthanum concentration measured by ICP-MS, both in 2D and 3D models, as shown Figure 5. These results confirmed the ability of LaF_3:Ce NPs to increase the radiation dose when sufficiently accumulated in cancer cells and highlighted the role of the coating in fulfilling this condition. The therapeutic effect obtained with nanoscintillators is probably due to multiple reactions. The physical RDE effect is followed by chemical reactions leading to the production of reactive oxygen species (ROS) in the culture medium, and biological reactions leading to tumor cell death and DNA damage. [48] Indeed, in the literature, in vitro and in vivo dose enhancement results have exceeded predictions made by Monte Carlo simulations, highlighting

the strong contribution of chemical and biological steps. In this study, the coating was shown to strongly impact cell internalization *in vitro* and consequently the ability of the NPs to enhance the radiation dose in 2D and 3D models of pancreatic tumors. However, this parameter is also critical to ensure proper *in vivo* biocompatibility of NPs. According to plasma biochemistry, intravenous injection of LaF_3:Ce NPs (200 $mg.kg^{-1}$) was well tolerated in mice with both coatings. It did not affect renal nor muscular functions, metabolism or nutritional status, and induced a mild hepatic toxicity after 14 days. Once injected, PEG- (≈ 45 nm) and TPP-coated NPs (≈ 257 nm) mainly accumulated in the liver and spleen, in line with the literature. While NPs smaller than 10 nm undergo renal clearance, NPs larger than a few tens of nanometers undergo hepatic clearance. [49] In accordance with their larger size, TPP-coated NPs accumulated more in the spleen compared to PEG-coated NPs. All these observations are coherent with previous *in vivo* studies of nanoscintillators in rodents that showed a preferential accumulation in the mononuclear phagocytic system. [30,50–56] Unlike TPP-coated NPs, PEG-coated NPs were progressively eliminated: lanthanum concentration measured in all organs was lower 14 days after injection compared to 24 hours. Thus, the safety profile of TPP-coated NPs is less appropriate than that of PEG-coated NPs for the treatment of pancreatic cancer by intravenous injection, due to their high and irreversible non-specific accumulation in liver and spleen. Because of their proximity to the pancreas, it would be difficult to specifically deliver X-rays to a pancreatic tumor without irradiating the liver and spleen that would thus get damaged. These results point out that despite more promising *in vitro* properties, TPP-coated NPs are less appropriate for *in vivo* applications. PEG-coated NPs circulated twice as long as TPP-coated NPs in the bloodstream and were associated with higher lanthanum concentration in the blood, reaching 25%ID.g^{-1} 5 minutes after injection compared to less than 1%ID.g^{-1} for TPP-coated NPs. A longer blood circulation time is generally associated with greater tumor accumulation through the EPR effect. [54,56] This result was confirmed when assessing biodistribution in nude mice bearing orthotopic pancreatic tumors. Lanthanum accumulation in the tumor 1 and 4 hours after injection was 2.3 times higher for PEG- than TPP-coated NPs, and 10 times higher 24 hours after injection. For other organs, a decrease in heart, lungs and kidney for PEG-coated NPs indicated an efficient elimination from non-specific organs, which is consistent with the first biodistribution study performed in healthy mice. For liver and spleen, a progressive accumulation was observed, which may be explained by a prolonged circulation time in the blood. On the contrary, no significant evolution was observed for TPP-coated NPs, in agreement with a much shorter circulation time. Because of their aggregation, TPP-coated

NPs may have been rapidly trapped in the liver and spleen, where more than 90%ID.g^{-1} of lanthanum was accumulated 1 hour after injection.

Thus, PEG-coated NPs are more biocompatible with less non-specific accumulation in healthy organs and a better elimination over time. They also exhibit a longer blood circulation time resulting in a better tumor accumulation, probably through EPR effect, making them more suitable for *in vivo* applications. These properties are in good agreement with the so-called stealth effect of PEGylated nanomaterials [40]. For future development, it is however important to remember that anti-PEG immunity is a real challenge, [57] as illustrated in a recent study that found that 56 to 72% of human serum samples presented anti-PEG antibodies. [58] For patients presenting anti-PEG immunity, the circulation time of the nanotherapeutics will be strongly impaired, [59,60] which may jeopardize the efficacy of the treatment. Alternative approaches based for example on poly(ethyl ethylene phosphate) are being investigated to guarantee stealth effect, while avoiding immunogenicity. [61]

Importantly, LaF_3:Ce NPs are only toxic under X-ray irradiation, as demonstrated *in vitro* where intracellular concentrations of lanthanum reached 1.4x10^{-5} µg.cell^{-1} and 1.5x10^{-6} µg cell^{-1} in PANC-1 and MIA PaCa-2 cells, respectively, without toxicity. Because radiotherapy can be spatially targeted, non-toxic accumulation in distant healthy organs can be tolerated. However, as previously discussed, accumulation in the liver and spleen following injection is problematic for pancreatic tumors because of the close proximity of these two organs. However, this may be less of a problem for tumors located further away from the spleen and liver, to which irradiation could be specifically delivered. Additionally, future studies will focus on improving nanoparticle biodistribution in order to improve intravenous administration and facilitate future clinical translation. However, if this goal is not achieved, intratumor delivery of LaF_3:Ce nanoparticles could be considered, using endoscopic delivery, as recently performed in human to deliver HfO_2 nanoparticles to a pancreatic tumor. [62]

LaF_3:Ce NPs have shown promising characteristics for cancer treatment due to their low intrinsic toxicity, significant radiation dose-enhancement and good biocompatibility profile. Therefore, they remain promising candidates for other poor-prognosis cancers, such as glioblastoma or ovarian cancer, which would benefit from the radiotherapeutic properties of nanoscintillators. However, for these two tumor types, different considerations may guide coating optimization, such as the ability to cross the blood brain barrier and the capacity to specifically accumulate in the tumor versus surrounding tissue. ~~For future studies, the use of PEG-coated NPs is recommended to reduce non-specific accumulation and increase tumor uptake.~~

4. Conclusion

Because they enhance radiation dose in several tumor models, LaF_3:Ce NPs are promising for X-ray activated therapies. This work confirms that their coating strongly impacts both *in vitro* and *in vivo* properties, by affecting internalization and therapeutic efficacy of the NPs. Additionally, it shows that despite lower *in vitro* treatment efficacy, PEG-coated NPs are better suited for therapeutic applications due to their improved biocompatibility properties. However, based on the biodistribution results, these NPs appear to not be relevant for intravenous injection for pancreatic cancer, but could hold promise for several other poor-prognosis cancers, such as glioblastoma or ovarian cancer and/or for alternative injection routes, including a direct injection in the pancreatic tumor. The question of the coating is also to consider in regard with future perspectives of nanoscintillators for X-ray induced photodynamic therapy or UV-radioluminescence induced DNA-damage that may require different intracellular distribution. Indeed, although intracellular localization of nanoscintillators may increase the efficacy of radiation dose-enhancement, which relies on electrons that can travel up to a few tens of micrometers, it may not be necessary. However, the intracellular localization of nanoscintillators may play a more important role for X-ray induced photodynamic therapy as the mean free path of the ROS produced, singlet oxygen for instance, is only of the order of a few nanometers. The proximity of the nanoparticles to the intracellular target may therefore be more crucial.

5. Methods

5.1. Synthesis of LaF_3:Ce NPs

5.1.1. Materials

All reagents (Lanthanide chlorides, purity: 99.99%, Jiayuan Advanced Materials Co., Ltd., China; Hydrofluoric acid, ≃50 wt. % in H_2O, Alfa Aesar, France), solvents (2-Pyrrolidinone, methyl alcohol, Sigma-Aldrich Chemie, France) and functionalizing molecules (Sodium tripolyphosphate (TPP), Sigma-Aldrich Chemie, France and PEO Phosphonic Acid, MW= 1000-1250 $g.mol^{-1}$., Specific Polymers, France) of reagent-grade quality were purchased and used without further purification.

5.1.2. Preparation of highly water-dispersible cerium-doped lanthanum fluoride NPs

10.36 g (0.0279 mol.) of lanthanum (III) chloride heptahydrate ($LaCl_3.7H_2O$) and 1.15 g (0.0031 mol.) of cerium (III) chloride heptahydrate ($CeCl_3.7H_2O$) were dissolved in 30 mL of

methyl alcohol (Solution A). In parallel, 2.43 mL (0.0698 mol.) of hydrofluoric acid were mixed with 124 mL of 2-Pyrrolidinone (Solution B). Solution A was quickly added to solution B, under magnetic stirrer. After 5 minutes stirring, a clear, colorless solution was obtained. The reaction medium was transferred into a Teflon-lined stainless-steel autoclave (Berghof, Germany, inner volume: ≈ 250 mL). The pressure vessel was sealed, heated and maintained for 1-hour at 170°C under stirring. After cooling, the resulting reaction crude was poured into ≈ 160 mL acetone. $La_{0.9}Ce_{0.1}F_3$ NPs precipitated immediately and completely as white flakes. These flakes were then isolated by centrifugation (8000 rpm, 20 min.). The slightly yellow supernatant was carefully removed and the light-brown centrifuged pellet was dispersed in 7 mL DI water using an ultrasonic bath. The NPs were precipitated again in 50 mL acetone. This process was repeated twice. The final light-brown pellet was dispersed in 6 mL DI water to obtain a transparent, slightly brown colloidal solution with a solid content of around 40% w/w.

5.1.3. $La_{0.9}Ce_{0.1}F_3$ nanoparticle (NP) functionalization

LaF_3:Ce NPs were functionalized to improve their dispersion in PBS, using molecules that present phosphonate or phosphate groups, which have an affinity for the NPs surface, enriched in lanthanide ions during synthesis (excess of Ln^{3+} ions compared to fluorine ions).

5.1.4. Polyethylene glycol (PEG) grafting

An aqueous colloidal solution at 10% weight was prepared and introduced under vigorous stirring into an aqueous solution containing PEO phosphonic acid (polyethylene glycol, 0.5 $mol.L^{-1}$). The Ln^{3+}/P molar ratio was equal to 3. The resulting perfectly transparent and slightly brown solution was heated for 1 hour at 80°C. After cooling, the solution was dialyzed. The purified NPs were recovered by lyophilization and dispersed in PBS with a NPs concentration of 35 $mg.mL^{-1}$.

5.1.5. Tripolyphosphate (TPP) grafting

An aqueous colloidal solution at 10% by weight was prepared. A 0.4 $mol.L^{-1}$ TPP aqueous solution was prepared and added with vigorous stirring to the colloidal solution. The Ln^{3+}/P molar ratio was equal to 1.6. The resulting brownish and opalescent solution was stirred at room temperature for 4 hours. The modified NPs were purified by ethanol precipitation, centrifugation, and dispersion in DI water. These steps were repeated three times before dispersing the final pellet in PBS with a final NP concentration of 35 $mg.mL^{-1}$.

5.2. Nanoparticle characterization

X-ray diffraction (XRD) patterns were recorded using a Malvern Panalytical Empyrean X-ray diffractometer (Cu-Kα radiation at 0.154184 nm) equipped with a Ni filter and a PIXcel3D detector. Data were collected in the 2θ range of 10-70°, with a scan speed of 0.5°.min^{-1} and a 0.02° step width.

TEM analyses were carried out using a JEOL JEM 2100F transmission electron microscope operating at 200 kV and equipped with a Gatan Ultrascan 1000 CCD camera and an Oxford X-Max 80 mm² energy dispersive spectrometer (EDS). Four different modes were used to characterize sample morphology, composition and structure: TEM and high-resolution TEM imaging, selected-area electron diffraction (SAED) and STEM-HAADF (wide-angle annular dark-field scanning transmission electron microscopy) imaging coupled with EDS. Samples were prepared by depositing the NPs on 300 mesh copper grids coated with an ultra-thin carbon film.

FT-IR analysis was performed using a PerkinElmer Spectrum 100 FT-IR spectrophotometer equipped with an attenuated total reflectance (ATR) sample chamber.

Thermogravimetric analyses were performed on a Setaram LABSYS1600 system.

Nuclear Magnetic Resonance experiments were performed on a Bruker Avance III 400 MHz spectrometer equipped with a Prodigy Cryoprobe. ^{1}H, ^{13}C and ^{31}P were acquired in deuterated water. Chemical shifts are given in ppm, using residual ethanol as a secondary reference. PEG and TPP molecules in deuterated water were also analyzed for comparison.

DLS measurements were performed using a Zetasizer Nano ZS (Malvern Panalytical). NPs solutions were diluted to reach 0.35 mg.mL^{-1} for the measurements in PBS and culture medium and 0.20 mg.mL^{-1} in mouse plasma. The parameters chosen for the analysis are described in **Table** .

	Viscosity (cP)	Refractive index	Dielectric constant
Culture medium + 10% FBS	0.94	1.345	80
Mouse plasma	1.25	1.351	100

Table 3. Parameters used for DLS analysis

Zeta potentials (ζ) were measured with a Zetasizer Nano ZS (Malvern Panalytical) at a concentration of 0.35 mg.mL^{-1} in PBS (pH = 7).

5.3. Cell culture

5.3.1. Materials

PANC-1 and MIA PaCa-2 human pancreatic cancer cells were obtained from the American Type Culture Collection (ATCC). The two cell lines were cultured in Dulbecco's Modified Eagle's Medium (DMEM, Gibco, 31966-021) supplemented with fetal bovine serum (FBS: 10%, Dominique Dutscher, 500105M1M) and penicillin/streptomycin (1%, Gibco, 15140-122), hereafter referred as complete medium. Cells were passaged twice a week at a 1:8 to 1:10 ratio, with passage number under 30, by using trypsin (trypsin-EDTA 0.5% (10X), Gibco, 15400-054). Cells were kept in a culture incubator maintained at 37°C, 5% CO_2.

The concentrations of LaF_3:Ce NPs given hereafter correspond to the final concentration in NPs in complete medium. For control conditions, the medium was replaced or supplemented with fresh complete medium without NPs.

5.3.2. Spheroid model

The spheroids were grown in suspension in round bottom ultra-low attachment plates (96-well, Corning). 5 000 cells were seeded per well in 100 µL medium in each well. The outer wells of the plate were filled with PBS to prevent evaporation. Cultures were maintained for 24 hours in the incubator to allow spheroid formation. NPs incubation was performed by replacing half of the culture medium by a 2X solution of LaF_3:Ce NPs.

5.4. X-ray fluorescence (XRF) microscopy and cryo-optical fluorescence microscopy

PANC-1 cells were seeded as adherent monolayers on silicon nitride membranes (Silson) deposited in the bottom of 4-well plates for 24 hours, and were incubated for another 24 hours with LaF_3:Ce NPs at 0.1 $mg.mL^{-1}$. After rinsing with PBS, the cells were incubated for 35 minutes at culture conditions with lysotracker green (50 nM, Invitrogen L7526) and Hoechst 33342 (2 drops per milliliter according to the manufacturer's instruction, NucBlue™, Invitrogen R37605). Cells were quickly rinsed with ammonium acetate buffer (150 mM), cryofixed (Leica, EM GP) and stored in liquid nitrogen until imaging. The vitrified cells were imaged at -185°C using a widefield cryo-fluorescence light microscope (Leica, Cryo CLEM), with a THUNDER Imager system equipped with a ceramic-tipped lens (NA = 0.9, 50X) using the brightfield and band pass filter cubes of green fluorescent protein (GFP, λ_{em} = 525 nm) and 4',6-diamidino-2-phénylindole (DAPI, λ_{em} = 477 nm). The distribution of physiological elements (*e.g.* Zn, P) and lanthanum was measured by X-ray fluorescence microscopy at the

ID16A beamline of the European Synchrotron Radiation Facility (ESRF, Grenoble, France). More details about the imaging parameters and analysis are provided in **SI.2**.

5.5. X-ray fluorescence microtomography

Spheroids of PANC-1 cells were grown in suspension for 24 hours as previously described, and incubated for another 24 hours with LaF_3:Ce NPs at 0.1 mg.mL^{-1}. Spheroids were rinsed with PBS, fixed in PFA and glued on 200 µm diameter quartz capillaries, as previously described [30]. X-ray fluorescence microtomography imaging was performed at the P06 beamline of the storage ring PETRA III (Deutsches Elektronen-Synchrotron DESY, Hamburg) (**Figure S11**). The samples were imaged after excitation with a monochromatic beam (14 keV), which was focused down to a size of about 450 nm x 300 nm (h x v) using Kirkpatrick-Baez mirrors. Images were acquired with a resolution of 5 µm/pixel, an acquisition time of 4 ms/pixel, and using 120 projections over 0° to 360.5° (acquisition time/spheroid ≈7 hours). For each scan point of the measurements, the XRF spectra were fitted using the non-linear least squares method implemented in the PyMca software. [63] The fitted XRF data were then sorted into image grids and quantified using calibration foils, either with known area density or in combination with parameters provided by the xraylib library, [64] according to the elements. Tomographic reconstruction of the quantified XRF data was performed using a maximum-likelihood expectation-maximization (MLEM) algorithm. [65] The final data provided the concentration for various elements including zinc (Zn), naturally present in cell nuclei and lanthanum (La).

5.6. TEM imaging on cells

PANC-1 and MIA PaCa-2 cells were grown as adherent monolayers on 2-well Lab-Tek™ (Thermo Scientific, 177380) for two days. Cells were incubated for 24 hours with 0.1 mg.mL^{-1} NPs. After incubation, the cells were washed with DMEM and fixed for 30 minutes in a solution containing 2% PFA (R1026) and 0.2% glutaraldehyde (GA, R1020) in DMEM with gentle shaking. After successive fixation, rinsing and staining steps as previously described, [66] cells were dehydrated in graded ethanol series, and embedded in Epon resin (Embed 812, Electron Microscopy Sciences, 14120). Ultrathin sections of 70 nm were cut on an ultra-microtome (Leica, UC7), collected on formvar-carbon coated copper 100 mesh grids (Formvar) and imaged with a Tecnai G2 Spirit BioTwin, with magnifications from 690X to 9300X.

5.7. MTS assay

7 500 cells/well were seeded in 96-well plates. After 24 hours, NPs were added to the cultures for 24 hours, with concentrations ranging from 0.01 to 20 mg.mL^{-1}. Untreated controls were prepared with complete medium and total killing controls were prepared by adding dimethyl sulfoxide (DMSO, 10%, Sigma-Aldrich, D4540). Cells were rinsed with PBS, and 100 µL of viability solution (CellTiter 96® Aqueous One Solution Cell Proliferation Assay, Promega, G3581) were added to each well already containing 100 µL of medium. After 2 hours incubation, the absorbance was measured at 490 nm with a CLARIOstar (BMG Labtech) plate reader.

5.8. X-ray irradiation of the cell cultures

X-rays were delivered by a CIX2 irradiator (Xstrahl) through a 3 mm aluminum filter; with the following parameters: voltage = 195 kV, current = 10 mA, and focal source distance (FSD) = 40 cm. The cell culture plates were placed at the center of the irradiation field to ensure a uniform radiation dose. The dose rate was measured using a PTW ionization chamber (TN30010-1) and a PTW UNIDOS E electrometer. The typical dose rate in water for these experiments was 1.8 ± 0.5 Gy.min^{-1}.

5.9. Clonogenic assay

Cells were seeded in T25 flasks and maintained in the incubator for 3 days. They were incubated for 1 hour with 2 mL of LaF_3:Ce NPs at 5 mg.mL^{-1} and irradiated as previously described. After irradiation, cells were rinsed three times with PBS, and collected using trypsin. Viable cells were counted with an automated cell counter (NanoEnTek EVE™) using trypan blue solution (0.4%, Invitrogen, T10282). 2 mL of complete medium was placed in each well of a 6-well plate, and cells were seeded at various densities according to the irradiation dose received (**Table)**. Cells were maintained at 37°C, 5% CO_2 for two weeks to allow the colonies to grow, with medium renewal when necessary. Colonies were then rinsed with PBS and incubated for 30 minutes with a staining solution of 0.5% crystal violet (Amresco, 0528) and 6% glutaraldehyde (Sigma-Aldrich, G6257) diluted in water. Plates were rinsed with water until the bottom was clear. Pictures were taken and analyzed using a custom-made ImageJ-based software.

5.10. Live/dead assay in 3D models

A live/dead assay was used to measure spheroid viability using a double staining based on calcein AM (live cells) and propidium iodide (PI, necrotic cells), as previously described. [46,67]

5.10.1. Toxicity in spheroids

Spheroids were grown as previously described and incubated for 24 hours with increasing concentrations of LaF_3:Ce NPs ranging from 0.01 to 20 $mg.mL^{-1}$ in culture medium. Control and NP-incubated spheroids were carefully rinsed twice by gently replacing 150 µL of the existing medium by the same volume of complete medium. A total killing (TK) group with 100% necrotic cells was prepared by fixing the spheroids for 2 minutes in formalin solution (10% neutral buffered, Sigma-Aldrich, HT5012). Spheroids were then rinsed with PBS and incubated with a 0.5% Triton solution (Triton® X-100, Bio-Rad, 161-0407) in PBS for 30 minutes to permeabilize the membranes. Spheroids were rinsed twice with a 0.1 $mol.L^{-1}$ glycine solution (Euromedex, 26-128-6405C) and maintained in PBS. After these steps, half of the medium was removed and replaced with the same volume of a live/dead staining solution (4 $\mu mol.L^{-1}$ calcein green AM, Invitrogen, C34852 and 6 $\mu mol.L^{-1}$ PI, Sigma-Aldrich, P4864) prepared in PBS. The plates were maintained in the incubator for 1.5 hours in the dark before being imaged using a confocal microscope (Zeiss, LSM510 Confocor II Combi) with a 5X objective (Plan Neofluar, NA = 0.15). The live (calcein) and dead (PI) signals were recorded at λ_{exc} = 488 nm / λ_{em} = 500–540 nm and λ_{exc} = 543 nm / λ_{em} = 600–670 nm, respectively. Image processing was performed using the custom-developed CALYPSO Matlab Code. [67]

5.10.2. Therapeutic efficacy in spheroids

Spheroids were grown as previously described and incubated for 24 hours with LaF_3:Ce NPs at 1 $mg.mL^{-1}$. Then, they were irradiated at 4, 8 or 12 Gy and rinsed twice by gently replacing 150 µL of the medium by the same volume of complete medium. Spheroids were carefully transferred using wide-orifice tips to new wells containing 200 µL of complete medium. Plates were maintained in culture conditions for 5 days. At that time, 145 µL of existing medium was removed to leave 50 µL of complete medium in each well. A 50 µL volume of live/dead staining solution prepared as previously described was added to each well. After 1.5 hours incubation, spheroids were imaged as previously described.

5.11. ICP-MS measurements on cell samples

Lanthanum and cerium concentrations were determined using quadrupole inductively coupled plasma mass spectrometry (ICP-MS, Perkin Elmer NexION 2000, Waltham, MA, USA). Adherent cells were seeded and grown following the clonogenic assay protocol. After NP incubation and rinsing steps previously described, cells were collected using trypsin,

centrifuged and counted. The cell pellet was resuspended in 500 µL PBS. Spheroids were seeded following the live/dead assay protocol. After NPs incubation, spheroids were rinsed as previously described, collected using large-orifice tips and manually dissociated to obtain a homogeneous cell suspension. Cells were counted, the suspension was centrifuged and the cell pellet was resuspended in 200 µL PBS. All samples were stored at -20°C until analysis. Samples were mineralized under atmospheric pressure in nitric acid for 24 hours at room temperature, followed by 3 phases of 8 hours in an oven (50°C) over 3 consecutive days. The mineralization was diluted to reach 1% concentration of nitric acid before analysis. Standard solutions were prepared in nitric acid 1% (v/v). ^{139}La and ^{140}Ce were measured; ^{103}Rh was used as an internal standard.

5.12. Animal experiments

All animal studies were performed in accordance with European guidelines and under the approval of the local ethics committee and the French Ministry of High Education and Research under the reference Apafis #32222-2022050416335097 v2. The animals were examined daily for general condition and behavior, and their weight was monitored three times a week. Humane endpoints were defined in advance to prevent, terminate or relieve animal pain or distress. Intravenous injections (200 µL) were performed at ≈200 µL.min^{-1} in the tail vein under isoflurane anesthesia (3%). Control groups received a PBS injection in the same conditions. Euthanasia was performed by cervical dislocation under 4% isoflurane anesthesia.

5.13.1. Toxicity

Six-week-old BALB/cJRj female mice (Janvier labs, France) received an intravenous injection of LaF_3:Ce NPs (200 µL, 200 mg.kg^{-1}), N = 5 animals/condition. Approximately 200 µL of blood was collected 24 hours and 14 days post-injection for plasma biochemistry analysis. Blood was centrifuged for 5 minutes at 10 000 rpm (20°C) to isolate the plasma. Samples were then kept at -80°C until analysis, which was performed using a M-Scan II (Melet Schloesing Laboratories) and the VET-16 reagent rotors that include markers of different physiological parameters. To measure NP biodistribution, mice were euthanized 24 hours or 14 days after injection. Organs (heart, liver, lungs, left kidney and spleen) were harvested, weighted and stored at -80°C. The organs were mineralized in 300 µL of concentrated HNO_3 and the lanthanum and cerium concentrations were measured by ICP-MS.

5.13.2. Pharmacokinetics

Six-week-old BALB/cJRj female mice (Janvier labs, France) received an intravenous injection of LaF_3:Ce NPs (200 µL, 200 $mg.kg^{-1}$), N = 3 animals/condition. Approximately 20 µL of blood were collected at the tail end; 5, 15, 30 minutes, 1, 2, 4, 8 and 24 hours post-injection. Blood samples were stored at -80°C until ICP-MS measurements.

5.13.3. Biodistribution

Six-week-old NMRI female nude mice (Janvier labs, France) were anesthetized (air/isoflurane 4% for induction, 2.5% during surgery) and Buprenorphine (0.1 $mg.kg^{-1}$) was injected subcutaneously. The left flank was incised and the spleen gently pulled out, exposing the pancreas. 1 million of Luciferase-expressing PANC-1 cells were resuspended in 50 µL Matrigel solution and orthotopically injected into the pancreas using a 29G syringe. After injection, the spleen and pancreas were repositioned and the different planes were sutured. Non-invasive bioluminescence imaging was performed 34 days after tumor cell injection (LUMINA III, PerkinElmer) to assess the presence of the tumor and randomize the animals in the different treatment groups (5 animals/group). All data are provided **Figure S.10**. 24 hours later, mice received an intravenous injection of LaF_3:Ce NPs (200 µL, 200 $mg.kg^{-1}$). Mice were euthanized 30 minutes, 4 hours or 24 hours after injection of NPs, and 30 minutes after PBS injection. Organs (heart, liver, lungs, left kidney, spleen and pancreas) and tumors were harvested, weighted and stored at -80°C until ICP-MS analysis for lanthanum and cerium quantification.

5.13. Statistical analysis and regression fits.

Statistical analyses were performed using GraphPad Prism version 9.2.0 (GraphPad Software, San Diego, California USA). All *in vitro* experiments were repeated independently at least twice. Results are presented as mean ± SEM (standard error of the mean). Student's t-test (two-tailed unpaired) was used to compare two experimental groups, especially PEG and TPP coatings for *in vitro* ICP-MS analysis. One-way analysis of variance (ANOVA) followed by Tukey post-hoc test was used for multiple-group comparison with one factor, in particular for the XRF microtomography experiments. Two-way ANOVA followed by Tukey post-hoc test was used for multiple-group comparison with two factors, including clonogenic and live/dead assays, as well as plasma biochemistry analysis. The threshold for statistical significance was set at a p-value below 0.05; (*) indicates $p < 0.05$, (**) indicates $p < 0.01$, and (***) indicates $p < 0.001$.

The non-linear regression fits for toxicity experiments (MTS for 2D models and live/dead assays for 3D models) were calculated according to the [inhibitor] vs response model, with

variable slope and four parameters. The half maximal inhibitory concentrations IC_{50} were calculated from the non-linear regression fits. The non-linear regression fits for clonogenic assays were calculated according to the linear quadratic cell death model. The linear regression fits for live/dead assays were calculated according to the simple linear regression model. The non-linear regression fits for blood pharmacokinetics experiments were calculated according to the two-phase decay model.

Supporting Information

Supporting Information is available from the Wiley Online Library or from the author.

Acknowledgements

The work was supported by grants from the Institut National de la Santé Et de la Recherche Médicale (INSERM) (CALYPSO project, INSERM Cancer), the Ligue Contre le Cancer Foundation, and the LABEX PRIMES of Université de Lyon (ANR-11-LABX-0063).

The design and analysis of the nanoparticles was done in the frame of the SCANnTREAT project, which received funding from the European Union's Horizon 2020 research and innovation program under grant agreement N° 899549.

We acknowledge the European Synchrotron Radiation Facility for provision of beamtime and we would like to thank the group from the ID17 and ID16A beamlines at ESRF, where part of the work was performed. Data from ID16A sessions correspond to the DOI 10.15151/ESRF-ES-440210815 and 10.15151/ESRF-ES-1028463280.

We acknowledge DESY (Hamburg, Germany), a member of the Helmholtz Association HGF, for the provision of experimental facilities. Parts of this research were carried out at the PETRA III beamline P06. Beamtime was allocated for proposal I-20210379 EC. This research was supported in part through the Maxwell computational resources operated at Deutsches Elektronen-Synchrotron DESY, Hamburg, Germany. The research leading to this result has also been supported by the project CALIPSOplus under the Grant Agreement 730872 from the EU Framework Programme for Research and Innovation HORIZON 2020.

This work used the platforms of the Grenoble Instruct-ERIC center (ISBG; UAR 3518 CNRS-CEA-UGA-EMBL) within the Grenoble Partnership for Structural Biology (PSB), supported by FRISBI (ANR-10-INBS-0005-02) and GRAL, financed within the University Grenoble Alpes graduate school (Ecoles Universitaires de Recherche) CBH-EUR-GS (ANR-17-EURE-0003). The IBS Electron Microscope facility is headed by Guy Schoehn and supported by the

Auvergne Rhône-Alpes Region, the Fonds Feder, the Fondation pour la Recherche Médicale and GIS-IBiSA.

The Optimal imaging platform is supported by France Life Imaging (French program "Investissement d'Avenir" grant; "Infrastructure d'avenir en Biologie Santé", ANR-11-INBS-0006) and the IBISA French consortium "Infrastructures en Biologie Santé et Agronomie".

The authors also thank Dominique André (Institut de Biologie et Pathologie, CHU Grenoble Alpes) for the ICP-MS analysis, Sylvain Caillat (Commissariat à l'Energie Atomique et aux Energies Alternatives) for his help during the irradiations, Marc-André Hograindleur (European Synchrotron Research Facility) for culturing the cells and Lucie Sancey as well as Benoit Busser (Institute for Advanced Biosciences) for the meaningful discussions regarding *in vivo* results.

Received: ((will be filled in by the editorial staff))

Revised: ((will be filled in by the editorial staff))

Published online: ((will be filled in by the editorial staff))

References

[1] P. Rawla, T. Sunkara, V. Gaduputi, *World J. Oncol.* **2019**, *10*, 10.
[2] A. McGuigan, P. Kelly, R. C. Turkington, C. Jones, H. G. Coleman, R. S. McCain, *World J. Gastroenterol* **2018**, *24*, 17.
[3] Y. Karakas, S. Lacin, S. Yalcin, *Expert Rev. Anticancer Ther.* **2018**, *18*, 51.
[4] T. Conroy, P. Pfeiffer, V. Vilgrain, A. Lamarca, T. Seufferlein, E. M. O'Reilly, T. Hackert, T. Golan, G. Prager, K. Haustermans, A. Vogel, M. Ducreux, *Ann. Oncol.* **2023**, *34*, 987.
[5] M. Palta, D. Godfrey, K. A. Goodman, S. Hoffe, L. A. Dawson, D. Dessert, W. A. Hall, J. M. Herman, A. A. Khorana, N. Merchant, A. Parekh, C. Patton, J. M. Pepek, J. K. Salama, R. Tuli, A. C. Koong, *Pract. Radiat. Oncol.* **2019**, *9*, 322.
[6] Gastrointestinal Tumor Study Group, *Cancer* **1987**, *59*, 2006.
[7] J. H. Klinkenbijl, J. Jeekel, T. Sahmoud, R. van Pel, M. L. Couvreur, C. H. Veenhof, J. P. Arnaud, D. G. Gonzalez, L. T. de Wit, A. Hennipman, J. Wils, *Ann. Surg.* **1999**, *230*, 776.
[8] J. P. Neoptolemos, D. D. Stocken, H. Friess, C. Bassi, J. A. Dunn, H. Hickey, H. Beger, L. Fernandez-Cruz, C. Dervenis, F. Lacaine, M. Falconi, P. Pederzoli, A. Pap, D. Spooner, D. J. Kerr, M. W. Büchler, European Study Group for Pancreatic Cancer, *N. Engl. J. Med.* **2004**, *350*, 1200.
[9] S. W. L. de Geus, M. F. Eskander, G. G. Kasumova, S. C. Ng, T. S. Kent, J. D. Mancias, M. P. Callery, A. Mahadevan, J. F. Tseng, *Cancer* **2017**, *123*, 4158.
[10] S. Myrehaug, A. Sahgal, S. M. Russo, S. S. Lo, L. M. Rosati, N. A. Mayr, M. Lock, W. Small, J. A. Dorth, R. J. Ellis, B. S. Teh, J. M. Herman, *Expert Rev. Anticancer Ther.* **2016**, *16*, 523.
[11] M. C. De Grandis, V. Ascenti, C. Lanza, G. Di Paolo, B. Galassi, A. M. Ierardi, G. Carrafiello, A. Facciorusso, M. Ghidini, *Int. J. Mol. Sci.* **2023**, *24*, 12681.
[12] P. Dawson, M. Penhaligon, E. Smith, J. Saunders, *Invest. Radiol.* **1988**, *23 Suppl 1*, S110.
[13] K. S. Iwamoto, S. T. Cochran, J. Winter, E. Holburt, R. T. Higashida, A. Norman, *Radiother. Oncol. J. Eur. Soc. Ther. Radiol. Oncol.* **1987**, *8*, 161.
[14] A. Norman, K. S. Iwamoto, S. T. Cochran, *Invest. Radiol.* **1991**, *26 Suppl 1*, S120.
[15] Z. Xu, T. Luo, J. Mao, C. McCleary, E. Yuan, W. Lin, *Angew. Chem. Int. Ed Engl.* **2022**, *61*, e202208685.

[16] M. Nakayama, R. Sasaki, C. Ogino, T. Tanaka, K. Morita, M. Umetsu, S. Ohara, Z. Tan, Y. Nishimura, H. Akasaka, K. Sato, C. Numako, S. Takami, A. Kondo, *Radiat. Oncol. Lond. Engl.* **2016**, *11*, 91.
[17] M. Salah, H. Akasaka, Y. Shimizu, K. Morita, Y. Nishimura, H. Kubota, H. Kawaguchi, T. Sogawa, N. Mukumoto, C. Ogino, R. Sasaki, *J. Exp. Clin. Cancer Res. CR* **2022**, *41*, 146.
[18] S.-W. Shin, W. Jung, C. Choi, S.-Y. Kim, A. Son, H. Kim, N. Lee, H. C. Park, *Mar. Drugs* **2018**, *16*, E510.
[19] D. Manoharan, L.-C. Chang, L.-C. Wang, Y.-S. Shan, F.-C. Lin, L.-C. Wu, H.-S. Sheu, W.-P. Su, C.-S. Yeh, *ACS Nano* **2021**, *15*, 9084.
[20] M. S. Wason, J. Colon, S. Das, S. Seal, J. Turkson, J. Zhao, C. H. Baker, *Nanomedicine Nanotechnol. Biol. Med.* **2013**, *9*, 558.
[21] A. Detappe, S. Kunjachan, L. Sancey, V. Motto-Ros, D. Biancur, P. Drane, R. Guieze, G. M. Makrigiorgos, O. Tillement, R. Langer, R. Berbeco, *J. Controlled Release* **2016**, *238*, 103.
[22] A. Alhussan, N. Palmerley, J. Smazynski, J. Karasinska, D. J. Renouf, D. F. Schaeffer, W. Beckham, A. S. Alexander, D. B. Chithrani, *Cancers* **2022**, *14*, 3586.
[23] W. Dong, Z. Cai, J. Pang, J. Wang, N. Tang, W. Zhang, F. Wang, Z. Xie, F. Lin, X. Chang, B. Qian, Y. Zhang, T. Lei, X. Han, *J. Biomed. Nanotechnol.* **2020**, *16*, 352.
[24] P. Seshacharyulu, M. J. Baine, J. J. Souchek, M. Menning, S. Kaur, Y. Yan, M. M. Ouellette, M. Jain, C. Lin, S. K. Batra, *Biochim. Biophys. Acta BBA - Rev. Cancer* **2017**, *1868*, 69.
[25] C. Dujardin, E. Auffray, E. Bourret-Courchesne, P. Dorenbos, P. Lecoq, M. Nikl, A. N. Vasil'ev, A. Yoshikawa, R.-Y. Zhu, *IEEE Trans. Nucl. Sci.* **2018**, *65*, 1977.
[26] W. Chen, J. Zhang, *J. Nanosci. Nanotechnol.* **2006**, *6*, 1159.
[27] W. Sun, Z. Zhou, G. Pratx, X. Chen, H. Chen, *Theranostics* **2020**, *10*, 1296.
[28] M. R. Squillante, T. Jüstel, R. R. Anderson, C. Brecher, D. Chartier, J. F. Christian, N. Cicchetti, S. Espinoza, D. R. McAdams, M. Müller, B. Tornifoglio, Y. Wang, M. Purschke, *Opt. Mater.* **2018**, *80*, 197.
[29] T. A. Tran, J. Kappelhoff, T. Jüstel, R. R. Anderson, M. Purschke, *Int. J. Radiat. Biol.* **2022**, *98*, 1484.
[30] A. Bulin, M. Broekgaarden, F. Chaput, V. Baisamy, J. Garrevoet, B. Busser, D. Brueckner, A. Youssef, J. Ravanat, C. Dujardin, V. Motto-Ros, F. Lerouge, S. Bohic, L. Sancey, H. Elleaume, *Adv. Sci.* **2020**, *7*, 2001675.
[31] E. Blanco, H. Shen, M. Ferrari, *Nat. Biotechnol.* **2015**, *33*, 941.
[32] M. J. Mitchell, M. M. Billingsley, R. M. Haley, M. E. Wechsler, N. A. Peppas, R. Langer, *Nat. Rev. Drug Discov.* **2021**, *20*, 101.
[33] M. A. Abakumov, A. S. Semkina, A. S. Skorikov, D. A. Vishnevskiy, A. V. Ivanova, E. Mironova, G. A. Davydova, A. G. Majouga, V. P. Chekhonin, *J. Biochem. Mol. Toxicol.* **2018**, *32*, e22225.
[34] E. Rozhina, A. Danilushkina, F. Akhatova, R. Fakhrullin, A. Rozhin, S. Batasheva, *J. Biotechnol.* **2021**, *325*, 25.
[35] Y. Portilla, Y. Fernández-Afonso, S. Pérez-Yagüe, V. Mulens-Arias, M. P. Morales, L. Gutiérrez, D. F. Barber, *J. Nanobiotechnology* **2022**, *20*, 543.
[36] A. Sharma, C. Cornejo, J. Mihalic, A. Geyh, D. E. Bordelon, P. Korangath, F. Westphal, C. Gruettner, R. Ivkov, *Sci. Rep.* **2018**, *8*, 4916.
[37] Y. Matsumura, H. Maeda, *Cancer Res.* **1986**, *46*, 6387.
[38] Q. Zhang, E. C. Pratt, R. Tamura, A. Ogirala, H.-T. Hsu, N. Farahmand, S. O'Brien, J. Grimm, *Nano Lett.* **2021**, *21*, 4217.
[39] D. Sun, S. Zhou, W. Gao, *ACS Nano* **2020**, *14*, 12281.
[40] K. Knop, R. Hoogenboom, D. Fischer, U. S. Schubert, *Angew. Chem. Int. Ed Engl.* **2010**, *49*, 6288.
[41] W. W. Moses, S. E. Derenzo, *Nucl. Instrum. Methods Phys. Res. Sect. Accel. Spectrometers Detect. Assoc. Equip.* **1990**, *299*, 51.
[42] L. G. Jacobsohn, A. Toncelli, K. B. Sprinkle, C. J. Kucera, J. Ballato, *J. Appl. Phys.* **2012**, *111*, 074315.
[43] D. R. Cooper, K. Kudinov, P. Tyagi, C. K. Hill, S. E. Bradforth, J. L. Nadeau, *Phys Chem Chem Phys* **2014**, *16*, 12441.
[44] S. A. Loutfy, H. M. A. El-Din, M. H. Elberry, N. G. Allam, M. T. M. Hasanin, A. M. Abdellah, *Adv. Nat. Sci. Nanosci. Nanotechnol.* **2016**, *7*, 035008.

[45] J. C. Roeske, L. Nunez, M. Hoggarth, E. Labay, R. R. Weichselbaum, *Technol. Cancer Res. Treat.* **2007**, *6*, 395.
[46] J. P. Celli, I. Rizvi, A. R. Blanden, I. Massodi, M. D. Glidden, B. W. Pogue, T. Hasan, *Sci. Rep.* **2014**, *4*, 3751.
[47] R. Delorme, F. Taupin, M. Flaender, J.-L. Ravanat, C. Champion, M. Agelou, H. Elleaume, *Med. Phys.* **2017**, *44*, 5949.
[48] L. R. H. Gerken, M. E. Gerdes, M. Pruschy, I. K. Herrmann, *Mater. Horiz.* **2023**, *10*, 4059.
[49] N. Hoshyar, S. Gray, H. Han, G. Bao, *Nanomed.* **2016**, *11*, 673.
[50] C. Zhang, K. Zhao, W. Bu, D. Ni, Y. Liu, J. Feng, J. Shi, *Angew. Chem. Int. Ed.* **2015**, *54*, 1770.
[51] W. Sun, T. Shi, L. Luo, X. Chen, P. Lv, Y. Lv, Y. Zhuang, J. Zhu, G. Liu, X. Chen, H. Chen, *Adv. Mater.* **2019**, *31*, 1808024.
[52] Z. Jiang, L. He, X. Yu, Z. Yang, W. Wu, X. Wang, R. Mao, D. Cui, X. Chen, W. Li, *ACS Nano* **2021**, *15*, 11112.
[53] Y. Dou, Y. Liu, F. Zhao, Y. Guo, X. Li, M. Wu, J. Chang, C. Yu, *Theranostics* **2018**, *8*, 5870.
[54] X. Zhong, X. Wang, G. Zhan, Y. Tang, Y. Yao, Z. Dong, L. Hou, H. Zhao, S. Zeng, J. Hu, L. Cheng, X. Yang, *Nano Lett.* **2019**, *19*, 8234.
[55] F. Ahmad, X. Wang, Z. Jiang, X. Yu, X. Liu, R. Mao, X. Chen, W. Li, *ACS Nano* **2019**, *13*, 10419.
[56] Q. Zhang, E. C. Pratt, R. Tamura, A. Ogirala, H.-T. Hsu, N. Farahmand, S. O'Brien, J. Grimm, *Nano Lett.* **2021**, *21*, 4217.
[57] Y. W. Kong, E. C. Dreaden, *Front. Bioeng. Biotechnol.* **2022**, *10*, 879988.
[58] Q. Yang, T. M. Jacobs, J. D. McCallen, D. T. Moore, J. T. Huckaby, J. N. Edelstein, S. K. Lai, *Anal. Chem.* **2016**, *88*, 11804.
[59] B.-M. Chen, T.-L. Cheng, S. R. Roffler, *ACS Nano* **2021**, *15*, 14022.
[60] M. F. S. Deuker, V. Mailänder, S. Morsbach, K. Landfester, *Nanoscale Horiz.* **2023**, *8*, 1377.
[61] X. Yu, H. Li, C. Dong, S. Qi, K. Yang, B. Bai, K. Peng, M. Buljan, X. Lin, Z. Liu, G. Yu, *ACS Nano* **2023**, *17*, 23814.
[62] A. F. Bagley, E. B. Ludmir, A. Maitra, B. D. Minsky, G. Li Smith, P. Das, A. C. Koong, E. B. Holliday, C. M. Taniguchi, M. H. G. Katz, E. P. Tamm, R. A. Wolff, M. J. Overman, S. Patel, M. P. Kim, C.-W. D. Tzeng, N. Ikoma, M. S. Bhutani, E. J. Koay, *Clin. Transl. Radiat. Oncol.* **2022**, *33*, 66.
[63] V. A. Solé, E. Papillon, M. Cotte, Ph. Walter, J. Susini, *Spectrochim. Acta Part B At. Spectrosc.* **2007**, *62*, 63.
[64] T. Schoonjans, A. Brunetti, B. Golosio, M. Sanchez del Rio, V. A. Solé, C. Ferrero, L. Vincze, *Spectrochim. Acta Part B At. Spectrosc.* **2011**, *66*, 776.
[65] P. P. Bruyant, *J. Nucl. Med.* **2002**, *43*, 1343.
[66] A. Tarantini, K. D. Wegner, F. Dussert, G. Sarret, D. Beal, L. Mattera, C. Lincheneau, O. Proux, D. Truffier-Boutry, C. Moriscot, B. Gallet, P.-H. Jouneau, P. Reiss, M. Carrière, *NanoImpact* **2019**, *14*, 100168.
[67] A.-L. Bulin, M. Broekgaarden, T. Hasan, *Sci. Rep.* **2017**, *7*, 16645.
[68] N. A. P. Franken, A. L. Oei, H. P. Kok, H. M. Rodermond, P. Sminia, J. Crezee, L. J. A. Stalpers, G. W. Barendsen, *Int. J. Oncol.* **2013**, *42*, 1501.

*Clémentine AUBRUN FULBERT *, Frédéric CHAPUT, Sarah STELSE-MASSON, Maxime HENRY, Benoit CHOVELON, Sylvain BOHIC, Dennis BRUECKNER, Jan GARREVOET, Christine MORISCOT, Benoit GALLET, Julien VOLLAIRE, Olivier NICOUD, Frédéric LEROUGE, Sandrine DENIS-QUANQUIN, Xavier JAURAND, Thibault JACQUET, Anthony NOMEZINE, Véronique JOSSERAND, Jean-Luc COLL, Jean-Luc RAVANAT, Hélène ELLEAUME [&] and Anne-Laure BULIN [&,*]*

Nanoscintillator coating: a key parameter that strongly impacts internalization, biocompatibility and therapeutic efficacy in pancreatic cancer models

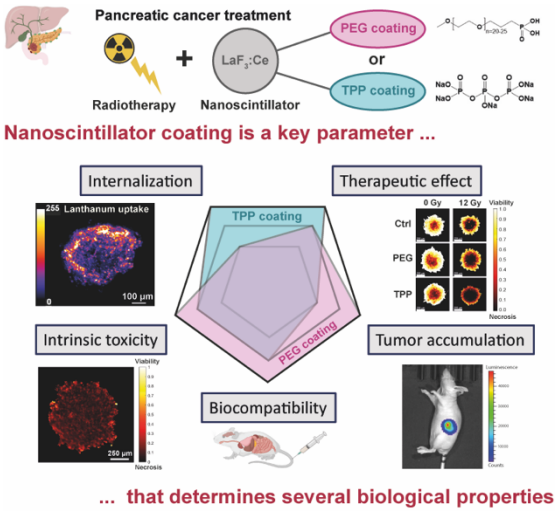

Nanoscintillators are innovative radiotherapeutics that can improve radiotherapy efficacy through various contributions, including radiation dose-enhancement. In this paper, we demonstrate that nanoscintillator coating drives biological properties, including internalization, which directly correlates with therapeutic efficacy, but also biocompatibility and biodistribution, in pancreatic tumor models. Preclinical studies show that a compromise can be reached between *in vitro* efficacy and *in vivo* biocompatibility.

Supporting Information

Nanoscintillator coating: a key parameter that strongly impacts internalization, biocompatibility and therapeutic efficacy in pancreatic cancer models

*Clémentine AUBRUN FULBERT *, Frédéric CHAPUT, Sarah STELSE-MASSON, Maxime HENRY, Benoit CHOVELON, Sylvain BOHIC, Dennis BRUECKNER, Jan GARREVOET, Christine MORISCOT, Benoit GALLET, Julien VOLLAIRE, Olivier NICOUD, Frédéric LEROUGE, Sandrine DENIS-QUANQUIN, Xavier JAURAND, Thibault JACQUET, Anthony NOMEZINE, Véronique JOSSERAND, Jean-Luc COLL, Jean-Luc RAVANAT, Hélène ELLEAUME [&] and Anne-Laure BULIN [&,]**

SI. 1. ^{31}P Nuclear Magnetic Resonance (RMN)

All samples were prepared in deuterated water.

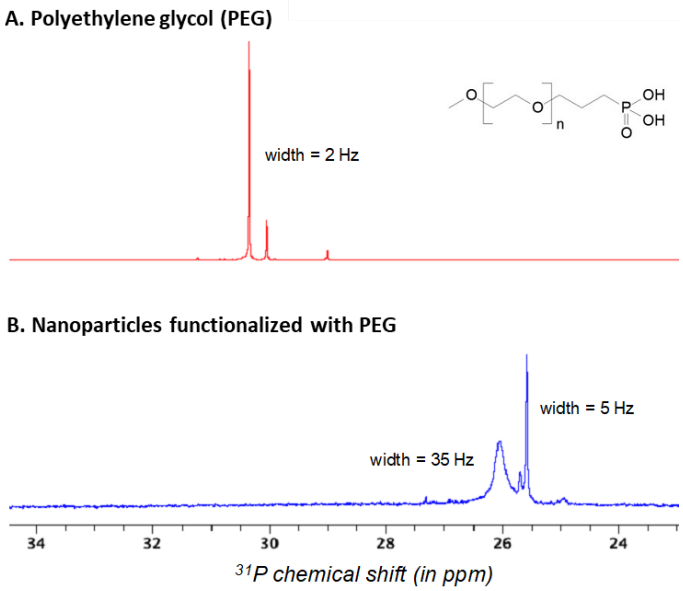

Figure S1. ^{31}P NMR spectra of polyethylene glycol (PEG, A) and LaF_3:Ce NPs functionalized with PEG (B).

PEG molecules exhibit one sharp signal at 30.5 ppm, whereas two signals are observed for functionalized NPs, at 26 and 25.5 ppm. The two signals are attributed to two binding modes of the phosphorus head on the surface, with probably one or two oxygens in interaction. The sharpness of the signals indicated non-covalent interactions.

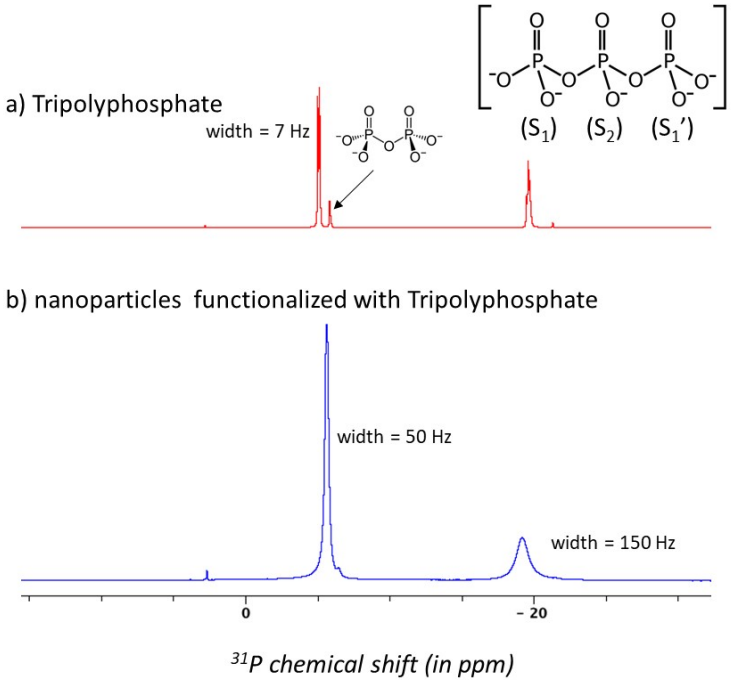

Figure S2. ^{31}P NMR spectra of tripolyphosphate (A) and LaF_3:Ce NPs functionalized with TPP (B).

TPP molecules exhibit two main signals at -5 and -19.5 ppm (presence of a weak signal at -5.8 ppm corresponding to pyrophosphate, here as an impurity), which were also observed for functionalized NPs with significant broadening, confirming the presence of the TPP on the nanoparticle surfaces. These signals can be assigned respectively to the terminal and middle phosphors of the TPP molecules. The NMR spectra suggest that the symmetry of the TPP molecule is preserved and no hydrolysis occurred during the reaction. Several coordination sites can be considered for the surface cations (S_1, S_2 or S_1'). Interaction with the nanoparticle surface takes place either through the S_2 site, leaving the P-O^- of the S_1 and S_1' sites free, or through the S_1 and S_1' sites, leaving the P-O^- of the S_2 site free. These coordination modes give the nanoparticles a negative surface charge, confirmed by zeta potential measurements in water at pH=7 (-45 mV). It should also be noted that solution NMR measurements do not allow the observation of aggregated NPs, their signals being broadened to the point of being indistinguishable from the baseline.

SI. 2. X-ray fluorescence microscopy

ID16A beamline is under high-vacuum to enable measurements on frozen hydrated samples at -153°C. A monochromatic X-ray beam (17 keV) was focused down to 40 nm using a pair of Kirkpatrick-Baez mirrors. The emission of fluorescence was recorded by two custom multi-

element Silicon Drift Detectors placed on both sides of the sample and facing each other at 90° from the incident X-ray beam. The resulting XRF spectra were fitted pixel by pixel (50 nm size, 50 ms dwell-time) using PyMca software [47] and the elemental areal mass concentration were calculated. Imaging a single cell took ≈ 4-5 hours. The correlative imaging between optical fluorescence microscopy and XRF elemental images was obtained using ec-CLEM plugin of Icy software.

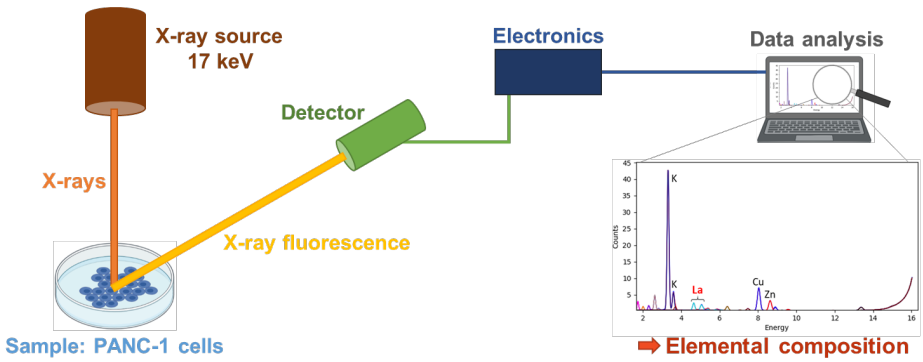

Figure S3. Schematic representation of X-ray fluorescence spectroscopy principle, as operated on ID16A, European Synchrotron Radiation Facility, Grenoble, France. Created with BioRender.com.

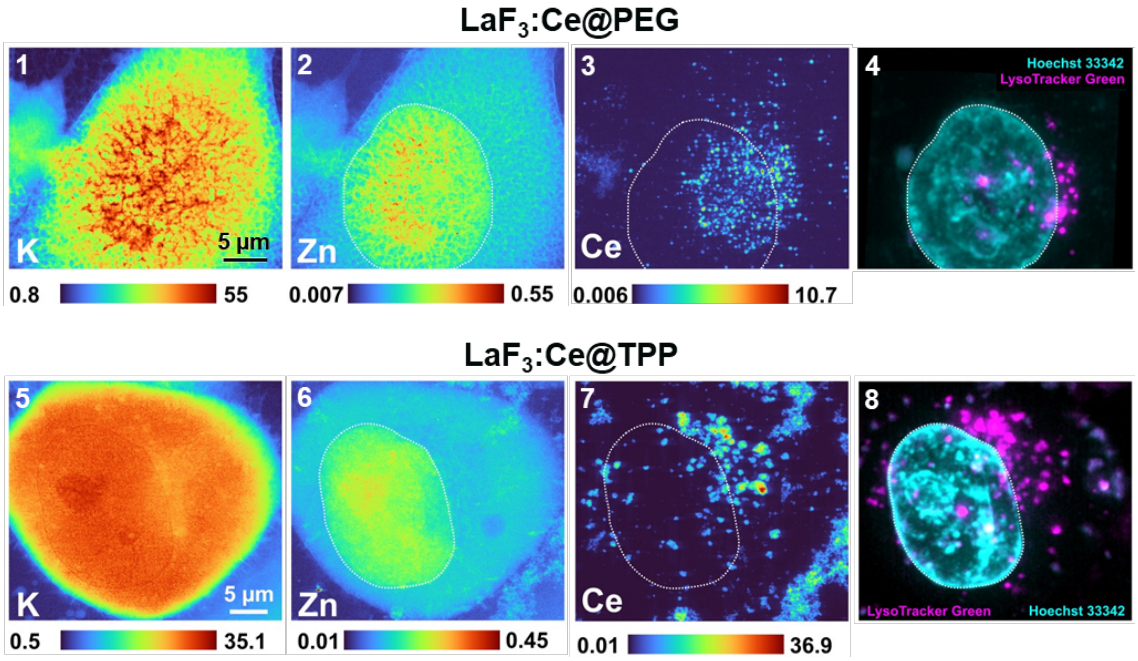

Figure S4. X-ray fluorescence spectroscopy images of PANC-1 cells incubated for 24 hours with LaF_3:Ce NPs at 0.1 mg.mL^{-1} (scale bar = 5 µm, ESRF, ID16), either with PEG (1-4) or TPP coating (5-8). Different elements are represented: 1, 5) potassium (cytoplasm), 2, 6) zinc (nucleus), 3, 7) cerium (NPs), 4, 8) Lysotracker Green (purple) and Hoechst 33342 (cyan).

SI. 3. ICP-MS results

		LaF_3:Ce@PEG		LaF_3:Ce@TPP	
2D models		24h, 1 mg.mL^{-1}	1 h, 5 mg.mL^{-1}	24 h, 1 mg.mL^{-1}	1 h, 5 mg.mL^{-1}
	PANC-1	1.81x10^{-5}	1.37x10^{-5}	6.40x10^{-5}	1.24x10^{-4}
	MIA PaCa-2	9.79x10^{-6}	1.47x10^{-6}	1.41x10^{-5}	9.11x10^{-5}
3D models		LaF_3:Ce@PEG		LaF_3:Ce@TPP	
		24 h, 1 mg.mL^{-1}		24 h, 1 mg.mL^{-1}	
	PANC-1	1.83x10^{-4}		1.30x10^{-2}	
	MIA PaCa-2	1.92x10^{-5}		2.33x10^{-3}	

Table S1. Intracellular lanthanum concentration (µg.cell^{-1}) measured in 2D and 3D models using ICP-MS

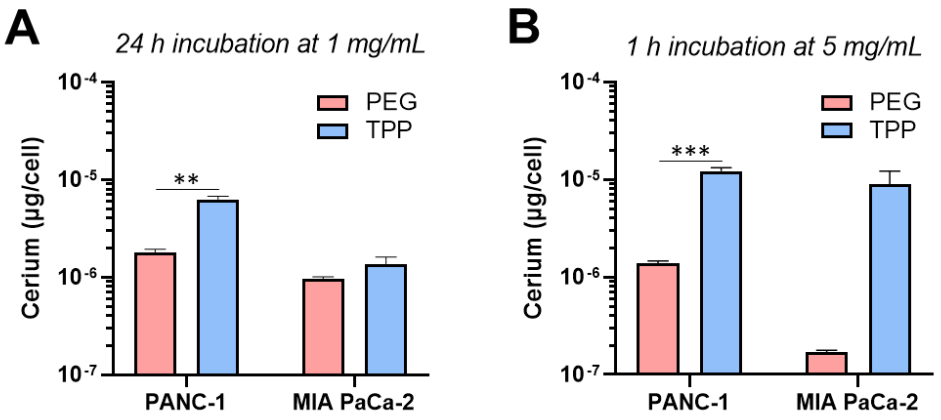

Figure S5. Concentrations of cerium measured by ICP-MS in PANC-1 and MIA PaCa-2 cells gown in 2D after incubations with LaF_3:Ce NPs: **A)** 24 hours at 1 mg.ml^{-1}, **B)** 1 hour at 5 mg.mL^{-1}.

SI. 4. Dose-enhancement factor (DEF)

SI.4.1 Experimental DEF calculation using clonogenic assays.

The survival plots of the control groups, normalized on the 0 Gy condition, were first fitted with the linear quadratic model (**Equation 1**), which provided the α and β parameters. The α (Gy^{-1}) parameter characterizes the initial slope of cell survival curves and low-dose efficacy, while β (Gy^{-2}) represents the increasing contribution of cumulative damage, assumed to be due to the interaction of two or more lesions. The α/β ratio represents the dose at which the two terms contribute equally to the effect [68], and are characteristic of each cell line.

$$\frac{S_{Controls}}{S_0} = e^{-(\alpha_c D + \beta_c D^2)} \qquad \textbf{Equation 1}$$

$\frac{S_{Controls}}{S_0}$ represents the normalized survival of the control cells, relative to 0 Gy; α_c (Gy^{-1}) and β_c (Gy^{-2}) are the characteristic parameters of each cell line, and D is the radiation dose (Gy).

We calculated the DEF assuming that the cells survival in presence of the nanoparticles was impaired only by a physical enhancement of the dose due to the presence of the NPs. The survival plots of the cells irradiated in presence of the NPs were fitted with **Equation 2** to extract the DEF, using the α and β parameters obtained from the control survival data of each cell line.

$$\frac{S_{nano}}{S_{nano,0}} = e^{-(\alpha_c.D.DEF+\beta_c.D^2.DEF^2)} \qquad \textbf{Equation 2}$$

$\frac{S_{nano}}{S_{nano,0}}$ is the normalized survival of the cells irradiated in presence of the NPs; α_c and β_c are the characteristic parameters of each cell line (described using equation 1) and D is the radiation dose (Gy).

SI.4.2 Experimental DEF from 3D live/dead assay.

To estimate the DEF from the experimental live/dead assay data performed on spheroids, the spheroid viability normalized on 0 Gy, plotted as a function of the X-ray dose were fitted with a linear model (**Equation 3**).

$$\frac{V}{V_0} = -\gamma . D \qquad \textbf{Equation 3}$$

Where $\frac{V}{V_0}$ is the viability of the cells normalized to the viability obtained at 0 Gy, γ (Gy^{-1}) the slope, and D is the radiation dose (Gy).

The DEF was obtained as the ratio of the slope of the viability plot obtained in presence of the NPs to the slope of the control curve for each cell line.

SI. 5. Therapeutic efficacy in 3D culture model

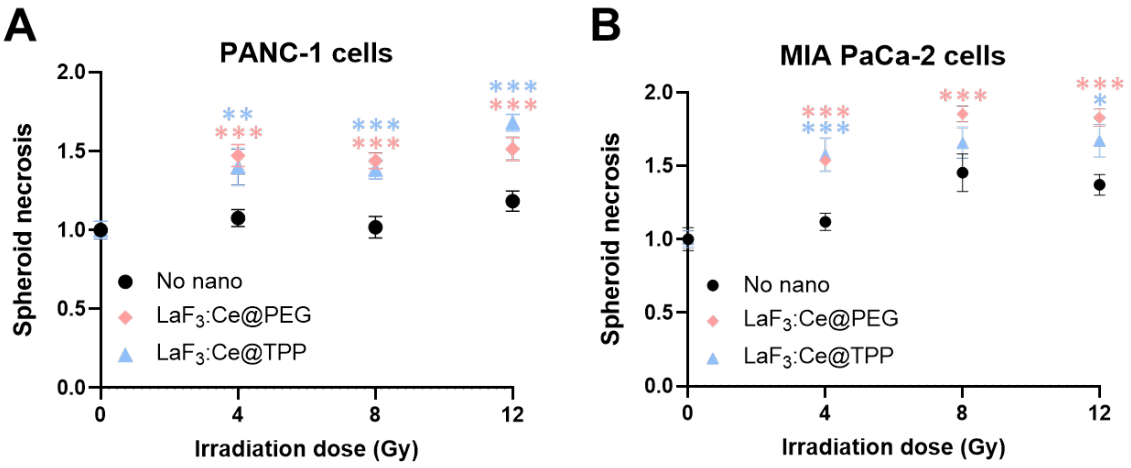

Figure S6. Spheroid necrosis plotted as a function of the irradiation dose for PANC-1 (A) and MIA PaCa-2 (B) cells. Data were normalized on the 0 Gy condition.

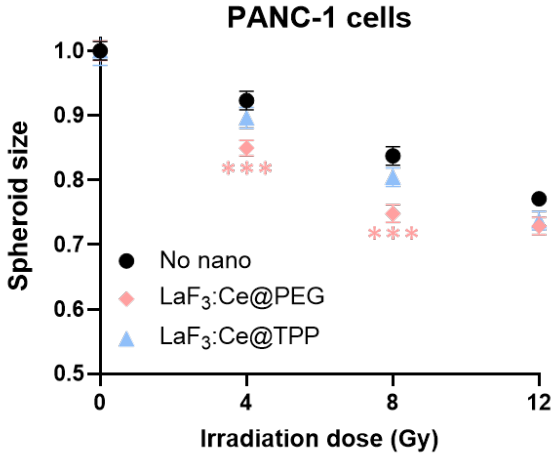

Figure S7. Size of the spheroids plotted as a function of the irradiation dose for PANC-1 spheroids. Data were normalized on the 0 Gy condition.

SI. 6. Animal monitoring

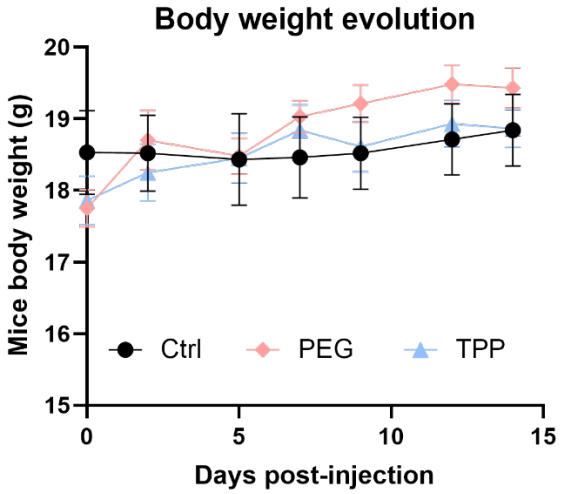

Figure S8. Body weight of BALB/c mice after intravenous injection of LaF_3:Ce NPs (200 $mg.kg^{-1}$, 200 µL), N = 5 mice/group.

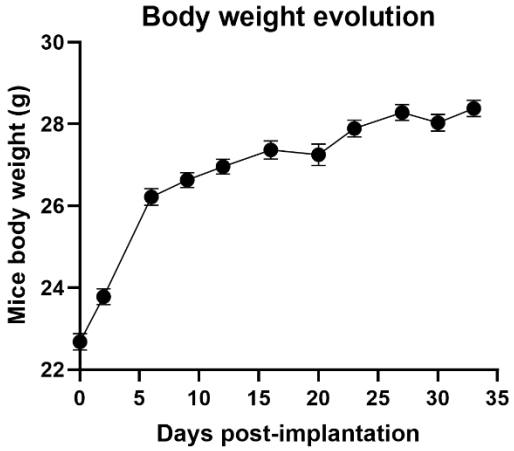

Figure S9. Body weight of NMRI nude mice after orthotopic implantation of pancreatic tumor cells, N = 5/group.

SI. 7. Randomization of the mice bearing orthotopically implanted pancreatic tumors for the biodistribution experiment

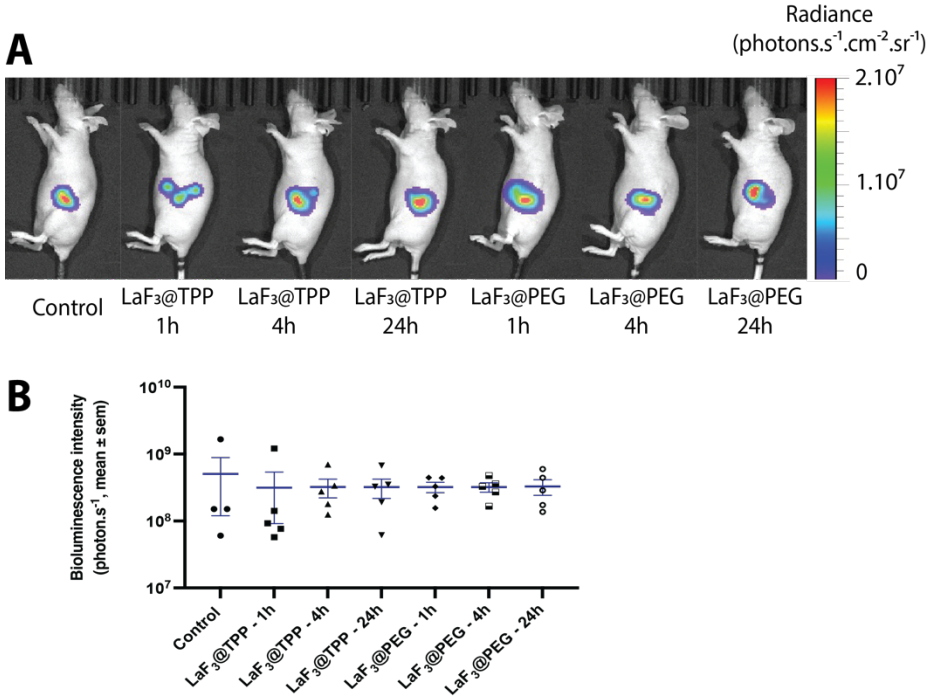

Figure S10. Animals baring orthotopically implanted pancreatic tumor were randomized using bioluminescence intensity measured 34 days post implantation (N = 5 mice/group). **A)** Representative images of mice bearing orthotopic pancreatic tumors 34 days post tumor implantation. **B)** The bioluminescence intensity was used to randomized the animals in each group.

SI. 8. X-ray fluorescence microtomography

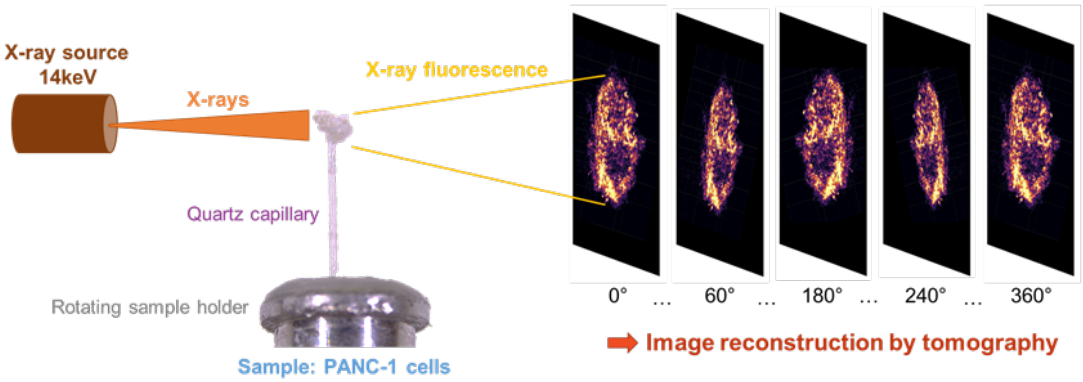

Figure S11. Schematic representation of X-ray fluorescence microtomography principle.

SI. 9. Experimental conditions for the clonogenic assays

	Dose (Gy)				
	0	1	2	3	4
PANC-1	200 / 250	225 / 275	450 / 550	800 / 1200	1800 / 2200
MIA PaCa-2	150 / 200	250 / 300	300 / 400	800 / 1200	1800 / 2200

Table S2: Number of cells seeded per well for various X-ray doses